Electrochemical Energy Reviews (2018) 1:1–34
https://doi.org/10.1007/s41918-018-0002-3

REVIEW ARTICLE

A Review of Carbon-Composited Materials as Air-Electrode Bifunctional Electrocatalysts for Metal–Air Batteries

Yan-Jie Wang[1,2,3] · Baizeng Fang[3] · Dan Zhang[1] · Aijun Li[1] · David P. Wilkinson[3] · Anna Ignaszak[4] · Lei Zhang[1,5] · Jiujun Zhang[1]

Received: 17 September 2017 / Revised: 9 December 2017 / Accepted: 27 January 2018 / Published online: 27 February 2018

Abstract
Metal–air batteries (MABs), particularly rechargeable MABs, have gained renewed interests as a potential energy storage/conversion solution due to their high specific energy, low cost, and safety. The development of MABs has, however, been considerably hampered by its relatively low rate capability and its lack of efficient and stable air catalysts in which the former stems mainly from the sluggish kinetics of the oxygen reduction reaction (ORR) and oxygen evolution reaction (OER) and the latter stems from the corrosion/oxidation of carbon materials in the presence of oxygen and high electrode potentials. In this review, various carbon-composited bifunctional electrocatalysts are reviewed to summarize progresses in the enhancement of ORR/OER and durability induced by the synergistic effects between carbon and other component(s). Catalyst mechanisms of the reaction processes and associated performance enhancements as well as technical challenges hindering commercialization are also analyzed. To facilitate further research and development, several research directions for overcoming these challenges are also proposed.

Keywords Metal–air batteries · Oxygen reduction reaction · Oxygen evolution reaction · Carbon · Bifunctional electrocatalysts · Synergistic effect

PACS 88.80.ff Batteries · 88.80.F– Energy storage technologies · 82.47.Aa Lithium-ion batteries

1 Introduction

Metal–air batteries (MABs), in particular rechargeable MABs, possessing high specific energy, low cost, and safety [1, 2], have gained great attention in recent years due to their feasibility as electrochemical energy storage/conversion solutions. A MAB system (see Fig. 1) is an electrochemical system consisting of a pure metal or metal alloy electrode for metal oxidation reactions (discharge process) and metal compound reduction reactions (charge process), as well as a second electrocatalyst coated air-electrode for oxygen reduction reactions (ORR, discharge process) and oxygen evolution reactions (OER, charge process). Between these two electrodes is an electrolyte serving as both a separator and an ion conductor [3]. Currently, the metal or alloy electrodes that have been developed in the fabrication of RMABs consist of Li, Zn, Al, Fe, Na, Ca, Mg, K, Sn, Si, Ge and/or their alloys [1, 4, 5] and typical catalysts of air electrodes include materials based on Pt, Ir, Ru and their alloys as well as various non-noble metals [6–10].

✉ Anna Ignaszak
Anna.Ignaszak@unb.ca

✉ Jiujun Zhang
jiujun@shaw.ca

1 School of Sciences, Institute for Sustainable Energy, Shanghai University, Shanghai 200444, China

2 School of Environment and Civil Engineering, Dongguan University of Technology, Dongguan 523808, Guangdong, China

3 Department of Chemical and Biological Engineering, University of British Columbia, Vancouver, BC V6T 1Z3, Canada

4 Department of Chemistry, University of New Brunswick, Fredericton, NB E3B 5A3, Canada

5 Energy, Mining and Environment, National Research Council Canada, Vancouver, BC V6T 1W5, Canada

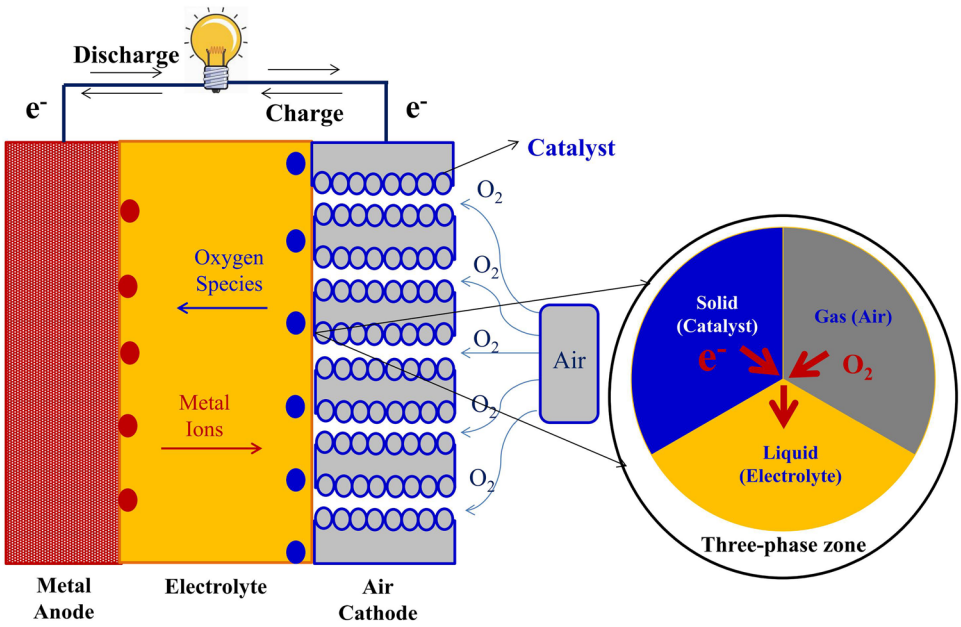

Fig. 1 A basic metal–air battery (MAB) configuration with a simplified solid–liquid–gas three-phase zone

Although MABs with oxygen in air possess drastically higher theoretical energy densities than traditional aqueous and lithium-ion batteries, the development and commercialization of MABs faces one major challenge: a lack of efficient and robust bifunctional air-electrode catalysts which significantly limits battery performance in terms of both rate capability and long-term stability [4, 6]. To overcome this challenge, global research of bifunctional air electrodes for MABs and in particular electrocatalysts for both ORR and OER has rapidly progressed in recent years. With respect to this, carbon materials have been employed as supports and components for catalysts to improve catalytic activity and stability.

Normally, the air-electrode catalyst layer for both ORR and OER is a matrix structure containing primarily of catalyst particles and/or carbon particle-supported catalyst particles and ionomers [4, 5, 11, 12]. To synthesize these catalysts and fabricate these catalyst layers, different nanotechnologies, associated characterization techniques as well as performance validation methods have been carried out to significantly optimize the morphology and surface area of these advanced nanostructured catalysts to obtain high catalytic activity and stability. As recognized, the interactions and synergetic effects between carbon and other components play an important role in performance optimization. Tailored designs and geometries of such carbon-composited bifunctional catalysts are also recognized as major factors in promoting catalytic activity and chemical/electrochemical stability. In addition, bi- or multi-carbon component catalysts can constitute new composites which not only possess original carbon characteristics but also present new properties for improving catalytic activity and stability.

With a focus on advanced carbon-composited materials as bifunctional electrocatalysts for rechargeable MAB air electrodes, this review examines the most recent progresses and research trends in both experimental and characterization strategies, providing up-to-date knowledge and information on MAB bifunctional catalysts. The reaction mechanisms of the catalytic processes, the catalyst component interactions in the presence of carbon, the synergetic effects induced by the addition of carbon into catalyst materials, as well as the relationship between physicochemical structure and catalytic performance are reviewed and analyzed. Current achievements and challenges in synthesizing catalysts and fabricating air electrodes are also summarized. Future research directions are also proposed in this review to accelerate research and development in this area to overcome challenges.

2 Composites of Different Carbons

Combinations of two different carbon materials have been previously reviewed and analyzed as modified carbon support materials for high-performance Pt-based fuel cell catalysts [13]. Here, based on the advantages of different carbon materials, formed carbon–carbon composite supports show enhanced ORR activities for Pt-based catalysts in polymer electrolyte membrane fuel cells (PEMFCs). Similar combinations of two or more different carbon materials have also been explored as metal-free bifunctional composite electrocatalysts for RMABs.

In regard to zero-dimensional carbon nanostructures with atomic sizes below 100 nm, graphene quantum dots (GQDs) exhibit satisfactory ORR performance due to strong quantum confinement, edge effects, and oxygen-rich functional groups on the material surface [14, 15]. By encapsulating

GQDs in a graphene hydrogel structure, Wang et al. [16] reported a carbon–carbon composite electrocatalyst in which the GQDs provided more active sites and the graphene hydrogel served as a conductive substrate to fix and sputter GQDs to prevent agglomeration and facilitate electron transfer. According to the proposed synthesis mechanism as shown in Fig. 2a, graphene quantum dot/graphene hydrogel (GH–GQD) composite samples are prepared and labeled as GH, GH-GQD-45, GH-GQD-90, GH-GQD-180, corresponding to GQD amounts of 0, 45, 90, and 180 mg. In the structural characterization of these GH-GQD samples, the combined results in typical SEM and TEM images (Fig. 2b–e) not only demonstrate the porous structure of the graphene hydrogel, but also indicate the existence of GQDs with different sizes ranging from 2 to 20 nm in the porous structure. For GQDs in particular, HRTEM images (Fig. 2f) proved the graphitization of carbon dots with no peaks being found at ~ 270 nm in the tested UV–Vis absorption spectra, confirming the presence of rich edges in the GQDs [15, 17]. At room temperature, the measured RDE results revealed that the GH–GQD composite samples exhibited better ORR activities than individual GH and graphene oxide because

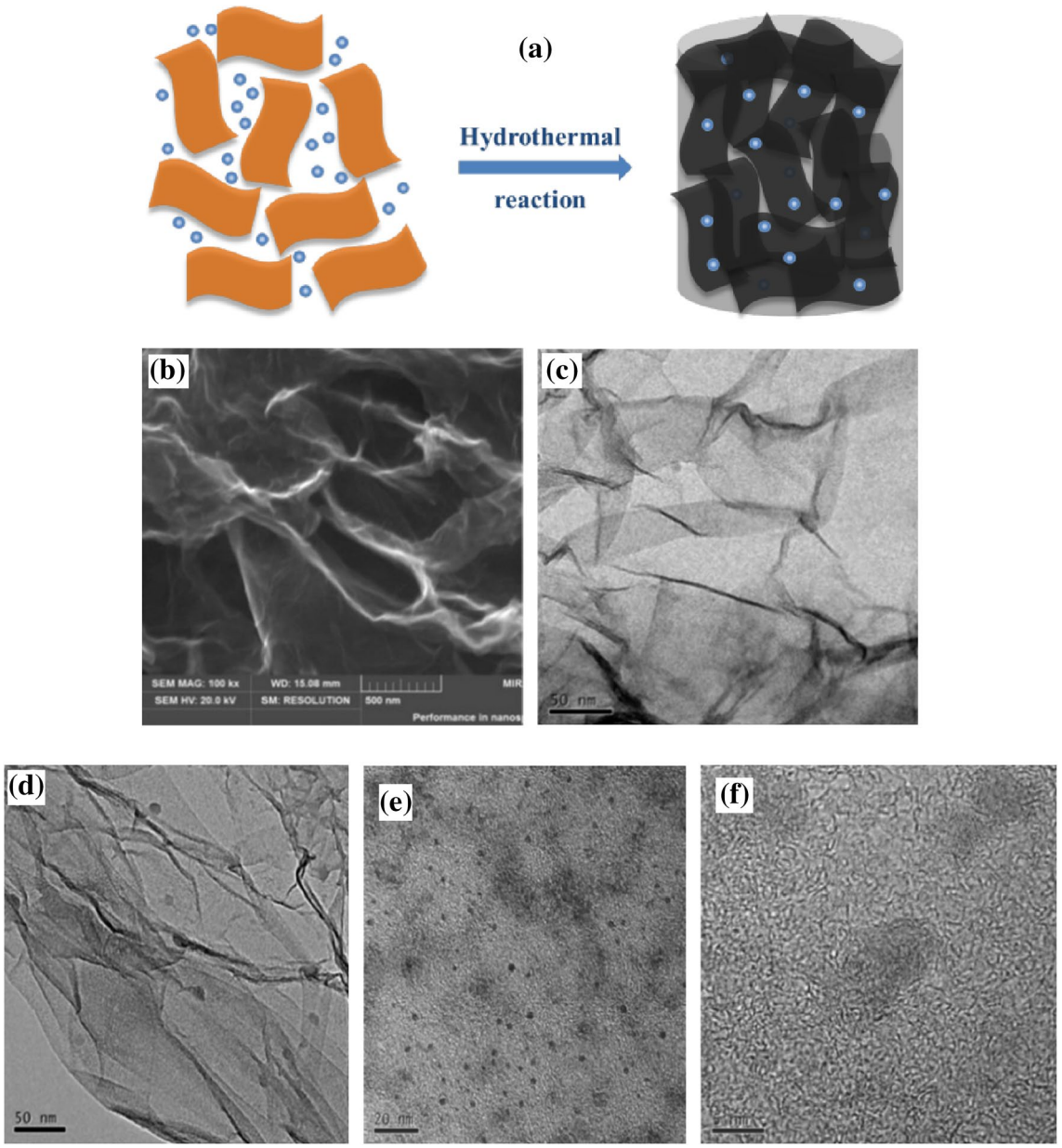

Fig. 2 **a** Illustration of the synthesis of GQDs, **b** SEM image of GQD-GH-90 with a scale bar of 500 nm, and TEM images of **c** GH, **d** GQD-GH-90, and **e** GQD, and **f** HRTEM image (scale bar = 5 nm) of GQDs. Reprinted with permission from Ref. [16]. Copyright 2016 Royal Society of Chemistry

of the synergistic effects between GH and GQDs in which GQDs provided more active sites and GH served not only as a conductive substrate for enhancing the charge transfer of electrodes, but also as a good support material conducive to the high dispersion of GQDs and their active sites. The GH-GQD-90 sample demonstrated the highest ORR onset potential of − 0.13 V among all GH–GQD composite samples, indicating that the optimized GQD amount is 90 mg. Linear sweep voltammetry (LSV) curves run in O_2-saturated 0.1 M KOH were used to evaluate the ORR mechanism, and it clearly demonstrated that the enhanced electrocatalytic activity resulting from the rich edge defects of the GH-GQD-90 composite sample was related to O_2 reactions through both two-electron and four-electron reaction pathways [18] as indicated by tested peroxide percentages and electronic transfer numbers. Interestingly, further investigations of GH-GQD-90 as a cathode electrocatalyst in a primary Zinc–air battery (ZAB) showed that the tested galvanodynamical discharging of the battery can increase to 100 mA cm^{-2}, demonstrating that GH-GQD-90 is an effective ORR catalyst that can provide sufficiently high battery performances. However, GH-GQD-90 only possessed comparable discharge properties to commercial 20 wt% Pt/C at higher current densities (~ 20 mA cm^{-2}) and no OER was discussed in the study. To further demonstrate the advantages of hybrid phases in the development of advanced carbon–carbon composite electrocatalysts in metal–air batteries (MABs) applications, Luo et al. [19] prepared composite cathode catalysts using Ketjan Black (EC-600JD)–carbon paper (KB/CP) in which the ultra-large specific discharge capacity of the KB/CP cathode in a lithium–air battery (LIB) was found to be much greater than that of individual KB and CP cathodes. This demonstrates that synergetic effects are present between the two different carbon components even if the two components have different structural morphologies and physical properties.

Aside from hybrid phases, core–shell structured composite catalysts have also been explored as MAB cathodes in which one carbon material acts as the core and the other carbon acts as the shell. To improve the electrochemical reactions of lithium–air batteries (LABs), Song et al. [20] designed and synthesized a carbon nanofiber@mesoporous carbon (CNF@mesoCs) core–shell composite catalyst to optimize the advantages and characteristics of two individual carbon materials. By coating mesoporous carbon onto carbon nanofibers (CNFs), the resulting structure not only enlarged surface areas but also provided a highly conductive graphitized surface to increase electrical conductivity. In their synthesis, CNFs were first produced as a core that entangled with one another to form a self-standing three-dimensional cross-linked web structure using electrospinning techniques. Nanocasting was then carried out to coat mesoporous carbon on to the CNFs to form the final CNF@mesoCs core–shell composite material. In their structural characterizations, the collected Raman spectra revealed that pristine CNFs possessed a lower peak ratio of D band to G band than CNF@mesoCs, indicating that the surface of CNF@mesoCs possessed a more graphitized structure than pristine CNFs. The CNF@mesoCs also displayed a better electrical conductivity of ~ 4.638 S cm^{-1} and a larger surface area of 2194 m^2 g^{-1} than pristine CNFs (~ 3.0759 S cm^{-1} and 708 m^2 g^{-1}), demonstrating the effects of mesoporous carbon onto CNFs in this CNF@mesoCs composite. The electrochemical performance of the CNF@mesoCs composite was also examined under an oxygen atmosphere in a discharging test using a fabricated LAB with non-aqueous electrolyte. Here, it was found that as the cathode, CNF@mesoCs demonstrated a higher discharge capacity (4000 mA h g^{-1}) than pristine CNFs (2750 mA h g^{-1}) because of its better electrical conductivity and larger mesopore size and volume. And although battery performances need to be further improved, this research provides a significant new design route to create advanced core–shell catalysts for LAB cathodes.

3 Composites of Carbon and Non-metals

3.1 Composites of Carbon and Single Elements

In this subsection, carbon materials composited with a non-metal heteroatom such as nitrogen (N), boron (B), or phosphorus (P) are reviewed. These non-metal heteroatoms are usually introduced into pure carbon to form RMAB air-electrode catalysts through doping strategies. As identified, dopants can act as a secondary phase; providing adsorption structures for charge transfer and improving electrocatalytic activities of ORR and/or OER [21, 22]. Recently, various carbon materials (e.g., porous carbon materials, CNT, graphenes, carbon fibers, carbon xerogel, carbon aerogel, nanocage carbons, carbon nano-onions) have been explored as heteroatom-doped carbon catalysts for BMABs and the results show that these composited carbon materials exhibit desirable characteristics such as desirable pore size/volume, large surface area, and high stability.

3.1.1 N-Doped Carbons

To promote electrochemical properties, the doping of heteroatoms is often used to modify the nature and chemical properties of pure carbon materials and obtain advanced metal-free carbon catalysts for RMABs. As a typical heteroatom, nitrogen (N) has become the most popular dopant to facilitate catalytic reactions of carbon-based composite cathodes because N has a larger electronegativity than carbon, a comparable atomic size to carbon, and five valence electrons for bonding with carbon atoms [23, 24]. Specifically,

N-doped carbon materials possess structural defects and can withdraw electrons from carbon atoms to enhance the conductivity of the carbon material and thus improve battery performance [25–29].

To develop favorable mesoporous structures and highly active carbon-based advanced catalysts for LAB cathodes, Sakaushi et al. [30] investigated ionic liquid (IL)-based mesoporous nitrogen-doped carbons (meso-NdCs) with a designed mesoporous structure. In their silica template assisted (Ludox HS40) carbonization method, ionic liquid (*N*-butyl-3-methylpyridinium dicyanamide) was used as the source of both N and C, and carbonization temperatures of 900 and 1000 °C were performed to prepare two samples: meso-NdC-900 and meso-NdC-1000 [29, 31]. In the structural characterizations, the measured broad XRD patterns and TEM images revealed typical characteristics of highly porous materials with an average pore diameter of ca. 8 nm as induced by defects at the carbon walls or irregular fragments [32]. Importantly, as shown in N1*s* XPS spectra (Fig. 3), three N species, such as pyridinic (398.3 eV), pyrrolic (399.4 eV), and graphitic (401.0 eV) nitrogen, result from increasing carbonizing temperatures, demonstrating increasing ratios of graphitic nitrogen. This correlates with XRD results in which meso-NdC-1000 gives two typical peaks at (002) and (101) that are associated with a higher degree of graphitization as compared with meso-NdC-900. Elemental analysis showed that meso-NdC-1000 possessed a higher N content of ca. 12 wt% than meso-NdC-900 (~ 6 wt%). Based on a combination of Ex-situ XRD measurements and charge–discharge tests in an assembled LAB cell (the cell use 0.5 M LITFSI in TEGDME (Aldrich) as the electrolyte and was measured in the potential range of 2.0–4.0 V versus Li/Li^+ at 100 and 200 mA g^{-1}), meso-NdC-1000 was found to possess a lower discharge overpotential of 0.3 V as compared with metal-based catalysts in LAB and the lowest charge overpotential of 0.45 V (Table 1). At 100 and 200 mA g^{-1}, meso-NdC-1000 also possessed specific discharge capacities of ca. 1750 and 1280 mAh g^{-1}, indicating acceptable rate capabilities in LABs. These results suggest that meso-NdC-1000 catalysts with

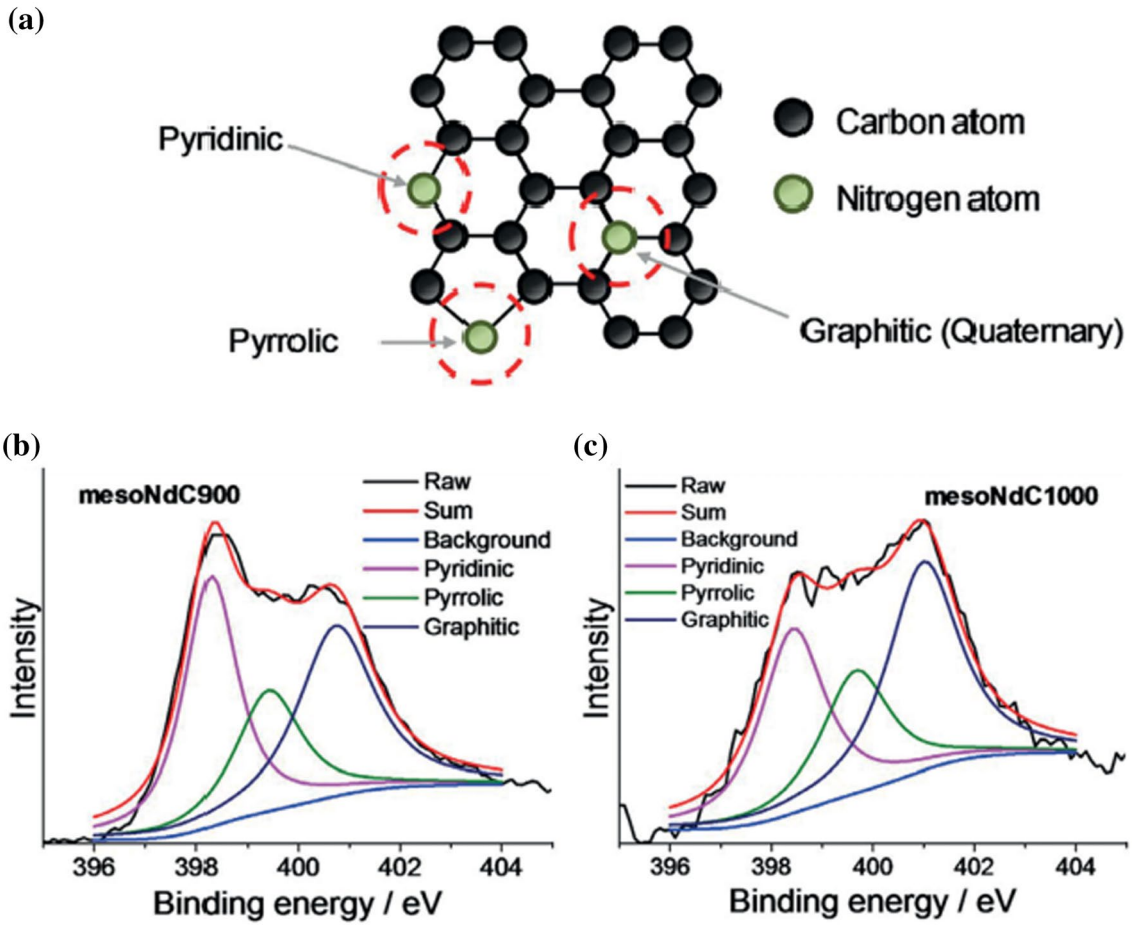

Fig. 3 **a** Schematic illustration of different chemical structures of doped nitrogen in a graphene framework. **b**, **c** X-ray photoemission spectra of meso-NdC-900 and meso-NdC-1000, with the peaks at 398.3, 399.4, and 401.0 eV corresponding to pyridinic, pyrrolic, and graphitic nitrogen respectively. Reprinted with permission from Ref. [30]. Copyright 2015 John Wiley and Sons

Table 1 Compared data on the electrochemical properties of several air electrodes. Reprinted with permission from Ref. [30]. Copyright 2015 John Wiley and Sons

Catalyst	η^{a}_{OER} (V)	Q_{disk} (mAh g^{-1})	I (mA g^{-1})	Electrolyte
Noble carbon	0.45	1750	100	1 M LiTFSI in TEGDME
Porous Au	0.6	325	500	0.1 M $LiClO_4$ in DMSO
Co_3O_4/*r*GO	0.6	14,000[c]	140	1 M $LiPF_6$ in TEGDME
TiC[b]	0.8	350	250	0.5 M $LiClO_4$ in DMSO
Co_3O_4/carbon	0.9	2000[c]	70	1 M $LiPF_6$ in PC
α-MnO_2/carbon	1.0	2500[c]	70	1 M $LiPF_6$ in PC
Carbon (Super-S)	1.8	850	70	1 M $LiPF_6$ in PC

[a]Comparison of average overpotentials@recharging (η_{OER}) for several catalysts to fully recharge a LAB. Here, overpotential (V) = $E_{OER} - 2.96$. E_{OER} (V vs. Li/Li^+) is the average reaction potential of a LAB at recharging, that is, an OER reaction. The value 2.96 (V vs. Li/Li^+) is the electromotive force of the following reaction: $O_2 + 2Li^+ + 2e^- \leftrightarrow Li_2O_2$. The η_{OER} data are selected from reports showing full discharge-recharge measurements

[b]$LiFePO_4$/carbon is substituted for Li metal anode for this measurement to supply Li^+. Other measurements use Li metal-based anodes

[c]Q_{disk} is calculated based on the mass of carbon

increased ratios of graphitic nitrogen at higher temperatures possess favorable structures induced by doped nitrogen in mesoporous carbon.

In addition to the N-doped mesoporous carbon materials discussed above, other N-doped mesoporous carbon materials have also been obtained for MAB cathode catalysts [33–38]. For instance, a novel hierarchical N-doped carbon ORR catalyst (labeled by N:C-MgNTA) with a graphitic shell was prepared by Eisenberg et al. [38]. These researchers employed an in situ templating method coupled with etching and pyrolysis to synthesize microporous, mesoporous, and macroporous structured catalysts. The coexistence of microporous, mesoporous and macroporous structures was demonstrated to provide short electron and ion transport paths and increased active surfaces, benefiting catalytic activities [39, 40]. Based on an investigation of electrocatalytic ORR in O_2- and N_2-saturated 0.1 M KOH solutions, the researchers found that the synthesized N:C-MgNTA exhibited more effective ORR activities with a $4e^-$ transfer mechanism and was more stable than commercial 20 wt% Pt/C or the undoped carbon reference sample. A spherical N-doped hollow mesoporous carbon (HMC) material was also obtained as an efficient ZAB cathode by Hadidi et al. [34], in which hollow and mesoporous carbon structures were combined with N-doping to obtain a novel carbon bifunctional electrocatalyst through polymerization and carbonization of dopamine on a sacrificial spherical silica (SiO_2) template. Here, both polydopamine (PDA) and F127 acted as excellent carbon sources and PDA afforded the doping of N. A combination of SEM, TEM and high-resolution TEM (HR-TEM) images revealed a hollow mesoporous sphere after the silica was removed in hydrofluoric acid solution. Carbon shells (ca. 21 nm ± 28%) were also formed after carbonization, revealing graphitic and amorphous domains. Linear sweep voltammetry (LSV) curves from − 0.8 to 0.05 V versus Hg/HgO in O_2-saturated 0.1 M KOH solution at an electrode rotating rate of 1600 r min^{-1} showed that HMC provided higher ORR kinetic-limiting current densities (~ − 4.95 mA cm^{-2}) than benchmark Pt/C catalysts (~ − 4.39 mA cm^{-2}) and more positive ORR onset potentials (ca. − 0.055 V) than Pt/C (ca. 0.001 V). In a ZAB with 6 M KOH assembled using a Zn electrode, a separator, and an air cathode, the HMC catalyst also provided a charge–discharge potential gap lower than that of 40 wt% Pt/C (~ 60%). These results highlight the merits of the structure-designed HMC material with its small charge–discharge voltage polarization and high stability over repeated cycling and provide new avenues to develop cost-effective, high-performance metal-free electrocatalysts for MABs. Interestingly, some groups [41, 42] have used biomass to create porous carbon cathode materials for MABs and have produced decent electrocatalytic activity and stability, as well as satisfactory battery performance.

Among N-doped graphene materials [43–45], a special N-doped three-dimensional graphene (N-3DG) cathode catalyst was designed and fabricated for LABs by He et al. [45]. In their study, melamine was selected as the nitrogen source due to its high nitrogen content and strong interactions with graphene oxide (GO) to avoid severe stacking in the structure of the graphene nanosheets (GNS) in 3DG. A combination of TEM and EDX mapping images of the N-3DG, coupled with SEM images, revealed a highly porous two-dimensional structure for the nitrogen-doped graphene nanosheets with a homogeneous distribution of carbon, nitrogen and oxygen elements. Further comparisons of the N-3DG and 3DG samples in N_2 adsorption–desorption analysis indicated that due to the relatively severe stacking of GNSs in the 3DG, more mesopores and micropores favoring fast O_2 diffusion and electrolyte infiltration were formed in the N-3DG than the 3DG. In XPS, the revealed pyridinic

N (~ 54%) was regarded as an effective N type to improve ORR in the graphene plane or edge because it can donate more available lone electron pairs for effective oxygen activation [46]. Furthermore, according to first-principle computations [47], carbon sheets with pyridine N were found to be more thermodynamically favorable in attracting Li^+ and lithiated pyridinic N can provide excellent active sites for O_2 adsorption and activation in the discharge process of LABs. During testing of the N-3DG and 3DG-based cathodes in a LAB, N-3DG demonstrated a higher ORR onset potential and a higher cathodic peak current, implying higher ORR activities than 3DG. At 50, 100, and 200 mA g^{-1}, the tested discharge capacities of N-3DG were 7300, 5110, and 3900 mAh g^{-1}, respectively, corresponding to average operating voltages at 2.67, 2.64, and 2.56 V. These were all higher than those of 3DG. In cycling performance measurements with a cutoff capacity of 500 mAh g^{-1} at 100 mA g^{-1}, the N-3DG cathode exhibited better cycling performances over 21 cycles with a more stable reversible capacity and a better initial round-trip efficiency of 65.9%, whereas 3DG only performed for about 8 cycles with an initial cycle round-trip efficiency of 60.7%.

Similar to porous carbon and graphene, CNTs [27, 48, 49], CNFs [50–52], and carbon papers [53] have also attracted much research interest in the development of N-doped carbon cathodes for MABs. Mi et al. [27] used a floating catalyst chemical vapor deposition (FCCVD) method to synthesize a N-CNTs composite material in which ethylene and melamine were used as the carbon and nitrogen sources. In a discharge capacity test at 100 mA g^{-1} using both carbonate-based (propylene, carbonate/ethylene, carbonate, PC/EC) and ether-based (1,3-dioxolane/ethylene glycol dimethyl ether) electrolytes, N-CNTs produced better discharge capacities in both electrolytes compared with CNTs. This is because of the better dispersion of N-doping and more available sites for O_2 adsorption and reduction, as well as a better electrical conductivity facilitating the reduction of kinetics during discharge. The enhancement of ORR activity after N-doping was attributed to three main reasons: improved conductivity, more nucleation sites around nitrogen and less aggregation of discharge products. CNFs and CPs were subsequently used as N-doped carbon cathode catalysts in MABs [50–53] and the nitrogen-doped CNFs tested as the air cathode in a liquid ZAB operating in ambient air produced a maximum power density of 185 mW cm^{-2} and a maximum energy density of ~ 776 Wh kg^{-1} with a high open-circuit voltage (1.48 V) [50]. The corresponding rechargeable liquid ZAB showed a small charge–discharge voltage gap (0.73 V at 10 mA cm^{-2}), high reversibility (initial round-trip efficiency of 62%) and stability (voltage gap increased to ~ 0.13 V after 500 cycles). Moreover, other flexible all-solid-state rechargeable ZABs using N-doped CNF films as a cathode displayed excellent mechanical and cycling stabilities with low overpotentials (a high discharge and low charge voltage of ~ 1.00 and 1.78 V at 2 mA cm^{-2}, respectively) and long cycle life (6 h, and can be recharged by the mechanical replacement of the Zn anode) even under repeated bending conditions. The synthesized N-dope CP cathodes were tested in an assembled LAB with a non-aqueous electrolyte (1 M lithium perchlorate in dimethyl sulfoxide) and produced a cyclability of more than 30 cycles at a constant current density of 0.1 mA cm^{-2}. The first discharge capacity reached 8040 mAh g^{-1} with a cell voltage of ~ 2.81 V at 0.1 mA cm^{-2}, and the coulombic efficiency was 81% on the first cycle at 0.2 mA cm^{-2}. These results indicate that N-doped CP materials are promising in the development of low-cost, versatile paper-based O_2 electrodes for LABs.

3.1.2 Other Heteroatom-Doped Carbons

Like nitrogen, other heteroatoms such as boron (B), phosphorus (P), sulfur (S), and fluorine (F) have also been selectively used as doped carbon materials for MABs to produce different physicochemical properties. In contrast to N, B possesses lower electronegativity (~ 2.04) than C (~ 2.55) [54], and if doped to carbon, B becomes an electron acceptor, inducing a positive charge and resulting in charged sites (B^+) that favor O_2 adsorption and thus increased ORR activity [55, 56]. To study the important effects of B-doping and to create sufficient active sites, researchers [54, 57, 58] have focused their attention on combining mesoporous carbon structures with B-doping to explore advanced metal-free carbon catalysts. For example, Shu et al. [57] prepared novel mesoporous boron-doped onion-like carbon (B-OLC) microspheres using nanodiamond and boric acid as C and B sources for rechargeable sodium–oxygen (Na–O_2) batteries. In their structural characterizations, a comparison of HRTEM images and selected area electron diffraction (SAED) patterns of their B-OLC and OLC samples revealed the existence of multilayered sp^2 fullerene shells forming a quasi-spherical onion-like nanoparticle with particle sizes of 5–8 nm. The appearance of the graphite ring (002) in the SAED patterns also confirmed the effective conversion of nanodiamonds into sp^2 carbon phases with an identified interlayer spacing (~ 0.34 nm) that did not change after B-doping [59, 60]. Based on the B 1*s* spectrum in XPS, six deconvoluted peaks were obtained at 185.5, 188.8, 190.2, 191.5, 192.9 and 194.8 eV, corresponding to B_4C, BC_3, BC_2O, BCO_2 and B_2O_3 respectively [61, 62]. The six species of B were also found in the XPS spectra of the referenced B-doped super P (B-Super P), confirming the successful doping of boron, in which B-super P possessed a lower content (~ 0.83 at%) than B-OLC (~ 5.47 at%). At 0.15 mA cm^{-2}, the obtained discharge/charge curves in an assembled sodium–air battery showed that compared with

OLC and B-Super P cathodes, the B-OLC cathode delivered a higher discharge capacity (~ 10,200 mAh g^{-1}) and a lower overpotential, demonstrating higher bifunctional activities toward ORR and OER. In the investigation of rate capabilities, it was found that at 0.6 mA cm^{-2}, B-OLC presented a discharge capacity of ~ 7455 mAh g^{-1}. This was nearly 40 times greater than that of Super P (~ 160 mAh g^{-1}) and about twice that of OLC (~ 3558 mAh g^{-1}). This enhanced rate capability was attributed to the synergistic effects between B doping, mesoporous structures and particle sizes of OLC. Interestingly, B-Super P produced similar battery performances compared to Super P. This is possibly because a low B doping content (~ 0.83 at%) produces no effects on super P. In a further examination of reversibility, cycling performance tests were conducted at 0.3 mA cm^{-2}, and B-OLC was found to possessed better cyclability (up to 125 cycles) than OLC (~ 56 cycles) and Super P (~ 6 cycles), demonstrating the combined effects of B-doping and mesoporous structures.

P is an electron donor even though the electronegativity of P (~ 2.19) is lower than C (~ 2.55), and the incorporation of P into carbon by P-doping is easier than that of N or B due to a much larger covalent radium [(107 ± 3) pm] than N [(71 ± 1) pm] and B [(84 ± 3) pm]. Similar to the combination of B-doping (or N-doping) and porous structures, P-doping is used in combination with porous structures in the development of carbon-containing bifunctional composite catalysts for MABs [63–65]. Using a sol–gel polymerization method followed by pyrolysis and P-doping, Wu et al. [63] developed a low-cost and highly active P-doped carbon xerogel electrocatalyst to examine the effects of P-doping and porous structures on ORR. In their synthesis, resorcinol and formaldehyde were used as the carbon sources and H_3PO_4 was used as the phosphorus source. The as-prepared samples were labeled as P-C-1, P-C-2, P-C-3, P-C-4 and P-C-5, corresponding to weight ratios of 1:10, 2:10, 3:10, 4:10, and 5:10 phosphoric acid to carbonized sample (Co–C). In their structure characterizations, a combination of XRD and Raman spectroscopy confirmed increased defects and disordered carbon after P-doping corresponding with increasing P contents from 0.78 to 3.56 at%. The P content measured by inductively coupled plasma-atomic emission spectroscopy (ICP-MS) were 0.78, 1.41, 1.64, 2.77, and 3.56 at% for P-C-1, P-C-2, P-C-3, P-C-4, and P-C-5 samples, respectively. In the P 2*p* spectra of XPS, two deconvolved contributions at 132.5 and 134.5 eV can be assigned to P–C bonding and P–O bonding [66, 67], respectively. The presence of P–O bonding confirms the formation of P–O–C in the forms of C_3PO, C_2PO_2, and CPO_3, indicating the successful doping of P [68]. In the examination of ORR at room temperature using rotating ring-disk electrode (RRDE) technique, the comparison of onset potential and diffusion limiting current density showed that the ORR activity increased significantly in the order: pure carbon < P-C-1 < P-C-2 < P-C-5 < P-C-4 < P-C-3. Moreover, P-C-3 possessed a shift of ~ 70 mV in the half-wave potential as compared with 20 wt% Pt/C. Tested LSVs in O_2-saturated 0.1 M KOH with a scan rate of 10 mV s^{-1} at different electrode rotating rates demonstrated that the P-C-3 catalyst provided an ORR electron transfer number of ~ 3.81, suggesting a four-electron reaction pathway for P-C-3 in ORR similar to 20 wt% Pt/C. According to DFT calculations, the amount of P-doping was critical in the improvement of ORR in P-doped carbon xerogels. Based on ORR behaviors in which ORR activity increased with increasing P content from 0.78 at% (P-C-1) to 1.64 at% (P-C-3) and then decreased with increasing P content from 2.77 at% (P-C-4) to 3.56 at% (P-C-5), the optimal P content should be 1.64 at%, providing maximum ORR activity.

To obtain optimal bifunctional catalysts, an important comparison of the different types of heteroatom-doping was conducted by Su et al. [58], in which N, B, and P were used to dope ordered mesoporous carbons (OMCs). The researchers found that improvements to charge transfer kinetics is strongly depended on the nature of the doped heteroatom. At a doping level below 1.0 at%, the ORR activity tested in alkaline solutions increased in the order of: N-OMCs < P-OMCs < B-OMCs. No data was reported for stability in their study, however. Another study was conducted by Zhang et al. [69] on heteroatom(s)-doped graphdiyne, in which the dopants were N, S, B, and F. However, this research only focused on the comparison between single heteroatom and dual atom-doped graphdiyne cathode materials. These will be discussed in the next section.

3.2 Composites of Carbon and Dual Elements

Compared with single heteroatom-doped carbon materials with ORR activities that are inferior to conventional Pt/C catalysts, especially in acidic media and neutral solutions, doped carbon materials with two or more selected heteroatoms have been predicted to further improve ORR activity due to the synergetic effects arising from the co-doping of two or more heteroatoms in carbon [70]. Based on the fact that co-doping N-doped carbon with a second heteroatom (e.g., B, S or P) may improve ORR activity [71–73], Zhang et al. [74] conducted a scalable fabrication of three-dimensional N and P co-doped mesoporous nanocarbons (NPMC foams) and investigated the OER of these co-doped carbon materials. In a template-free method, three N, P co-doped mesoporous carbon (NPMC) foams (i.e., NPMC-900, NPMC-1000, and NPMC-1100) were prepared at annealing temperatures of 900, 1000, and 1100 °C, respectively. TEM images coupled with elemental mapping for the typical NPMC-1000 sample revealed a uniform distribution of C, N and P. A combination of XRD, Raman spectra, and

TEM indicated that pyrolysis can resulted in a majority of the thermally stable graphic carbon domains being occupied by the co-dopants of N and P from the PANI and phytic acid. Moreover, many edge-like graphitic structures were found in the HRTEM images of the examined NPMC-1000 sample which oversaw active sites and thus catalytic activity. It was found that these NPMC samples possessed three-dimensional mesoporous structures with large surface areas, high pore volume and suitable pore sizes for electrocatalytic activity. Both the existence of the four N species (i.e., pyridinic, pyrrolic, graphitic, and oxidized pyridinic N) and the two P-related bonds (i.e., P–C and P–O) [75] observed in XPS confirmed the successful doping of N and P heteroatoms into the carbon network through thermal pyrolysis. Based on further LSV curves obtained at 1600 r min^{-1} in O_2-saturated 0.1 M KOH solution with a scan rate of 5 mV s^{-1}, NPMC-1000 was found to provide the best ORR activity with comparable onset potentials (~ 0.94 V) and half-wave potentials (~ 0.85 V) to Pt/C. Although NPMC-900 possessed a higher N and P content than NPMC-1000, the relatively low pyrolysis temperature led to a possible higher charge transfer resistance and thus relatively poorer electrocatalytic activity. As for NPMC-1100, the removal of doped heteroatoms at higher temperatures (~ 1100 °C) resulted in a decrease in active sites and therefore a decrease in overall electrocatalytic activity. For OER, NPMC-1000 and NPMC-1100 samples displayed lower onset potentials and higher currents, demonstrating better OER activities than Pt/C. Compared with RuO_2 nanoparticles, NPMC-1000 electrodes exhibited lower onset potentials but less current densities at greater potentials. Interestingly, as a cathode material in primary and rechargeable ZABs, NPMC-1000 primary batteries demonstrated an open-circuit potential of 1.48 V with a specific capacity of 735 mAh g_{Zn}^{-1} (corresponding to an energy density of 835 Wh kg_{Zn}^{-1}), a peak power density of 55 mW cm^{-2} (at a current density of ~ 70 mA cm^{-2}), and stable operations for 240 h after mechanical recharging. For NPMC-1000 rechargeable ZABs, the battery cycled stably for 180 discharge/charge cycles over a period of 30 h at 2 mA cm^{-2}. According to DFT calculations, these tested battery performances are induced by the synergistic effects of N, P co-doping along with graphene edges for the improvement of bifunctional electrocatalytic activity toward OER and ORR [76].

Compared with N, P co-doping, N, B co-doping into carbon materials is more difficult because of the formation of by-products (e.g., hexagonal boron nitride, *h*-BN) during doping that can act as inert de-activating agents that reduce the electrochemical activity of catalysts [77]. To incorporate heteroatoms at select sites of graphene frameworks and prevent the formation of inactive by-products, Zheng et al. [78] prepared a B, N co-doped-graphene (B, N-graphene) catalyst using a two-step doping strategy in which NH_3 and H_3BO_3 were used as the N and B sources. In their investigation of co-doping, a combination of TEM, SEM, electron energy loss spectroscopy (EELS), and elemental mapping confirmed the uniform distribution of B and N in a preserved graphene nanosheet morphology, and FTIR revealed the existence of B and N coupled to C, indicating that by-products such as *h*-BN did not exist in the synthesized B, N-graphene sample. This was also confirmed by XPS in which a one-step synthesized *h*-BN/graphene reference sample clearly showed the *h*-BN phase. Cyclic voltammetry curves measured in an O_2-saturated 0.1 M KOH showed that B, N-graphene possessed a higher cathodic current density, indicating better ORR activity than *h*-BN/graphene. A series of LSVs in O_2-saturated 0.1 M KOH solution were collected using a RDE technique, and it was observed that the onset potential of B, N-graphene was closer to commercial Pt/C and higher than the one-step synthesized single heteroatom-doped graphenes (such as N-graphene and B-graphene). These results suggest that the co-doping of B and N can result in higher synergistic activities than single heteroatom-doped graphene and that N-doping in N-graphene is more effective on the improvement of activity than B-doping in B-graphene. RDE experiments at different rotation rates ranging from 500 to 2500 r min^{-1} revealed an electron transfer number (~ 3.97) for B, N-graphene similar to commercial Pt/C (~ 3.98) and a RRDE technique was further used to confirm the ORR pathway. Importantly, their DFT calculations revealed significant synergistic effects resulting from the coupling interactions between pyridinic N (one of N species) and B.

Similar to N and P, oxygen (O) also possesses higher electronegativity than carbon. Based on the effects of co-doping, Li et al. [23] developed a novel 3D O, N co-doped carbon nanoweb (ON-CNW) material as a metal-free catalyst for hybrid LABs. In the deconvolution of N1*s* and O1*s* spectra of XPS, the content of pyridone/pyrrolic on ON-CNW was about three times that of a referenced N-doped carbon nanoweb (N-CNW) material. The pyridone nitrogen was reported to stabilize singlet dioxygen by forming a stable adduct, weakening and breaking the bond in the oxygen molecule [79, 80] so that the activation process using KOH can further improve ORR activity. CV measurements using N-doped carbon nanosphere (N-CNS) catalysts were run in O_2-saturated 0.1 M KOH, and only a single ORR peak potential (~ 0.4 V) was observed. This peak was weaker than that of N-CNW(~ 0.29 V), indicating a difference in morphology and structure for the two PPY-derived carbon materials. The N-CNS was also found to possess greater particle resistance and reduced mass transport in the packed carbon spheres, whereas the 3D interconnected N-doped carbon fibers in the N-CNW increased electron transport, oxygen transport and electrolyte diffusion. In a further comparison of ORR peak potentials, ON-CNW presented a positive shift possibly due to a higher pyridone/pyrrolic content (~ 20.14%).

The N-CNW and ON-CNW samples were subsequently evaluated as cathode catalysts in an assembled hybrid LAB and the discharge voltage profiles of the cell revealed an apparent reduction in the difference between ON-CNW and Pt/C samples, demonstrating that ON-CNW possessed performances close to that of Pt/C catalysts. At 0.5, 1.0, 1.5, and 2.0 mA cm^{-2} (Fig. 4a). the discharge plateau of ON-CNW is lower than that of Pt/C but higher than those of acetylene black and N-CNW, suggesting that ON-CNW possesses higher ORR activities than N-CNW and carbon black. A compared cycling test was carried out in a hybrid LAB with a constant current density of 0.5 mA cm^{-2} and the round-trip overpotential for N-CNW (Fig. 4b) increased from 1.00 to 1.43 V, whereas ON-CNW (Fig. 4c) increased from 0.92 to 1.02 V, demonstrating the improved effects of O, N co-doping on activity and stability, and also confirming that ON-CNW is a promising ORR catalyst in hybrid LABs.

The co-doping of N and S [81–83] has also been demonstrated to provide benefits in the redistribution of spin and charge densities and the formation of more ORR active sites. To obtain simultaneous optimization of both porous structures and surface functionalities of N and S co-doped carbon, Wu et al. [81] designed and fabricated a polyquaternium-derived heteroatom (N and S) co-doped hierarchically porous carbon (N-S-HPC) catalyst for ORR using a simple, large-scale and green synthetic route with the assistance of a silica template. In their electrochemical evaluation of ORR, the LSV curves in O_2-saturated 0.1 M KOH at 1600 r min^{-1} with a scan rate of 5 mV s^{-1} and a catalyst loading of 500 μg cm^{-2} were recorded and compared. Compared with the two referenced samples [N-doped hierarchically porous carbon (N-HPC) and N, S-doped porous carbon (N-S-PC)], N-S-HPC presented a higher onset potential (~ 0.99 V) and a higher half-wave potential (~ 0.86 V), demonstrating higher ORR activity. In particular, even at a low catalyst loading of 100 μg cm^{-2}, N-S-HPC still exhibited a better half-wave potential (~ 0.83 V) and a greater diffusion-limited current density (~ 7.5 mA cm^{-2}) than those of commercial 20 wt% Pt/C (~ 0.82 V, ~ 5.5 mA cm^{-2}), suggesting that N-S-HPC possesses comparable ORR performance to Pt/C in alkaline

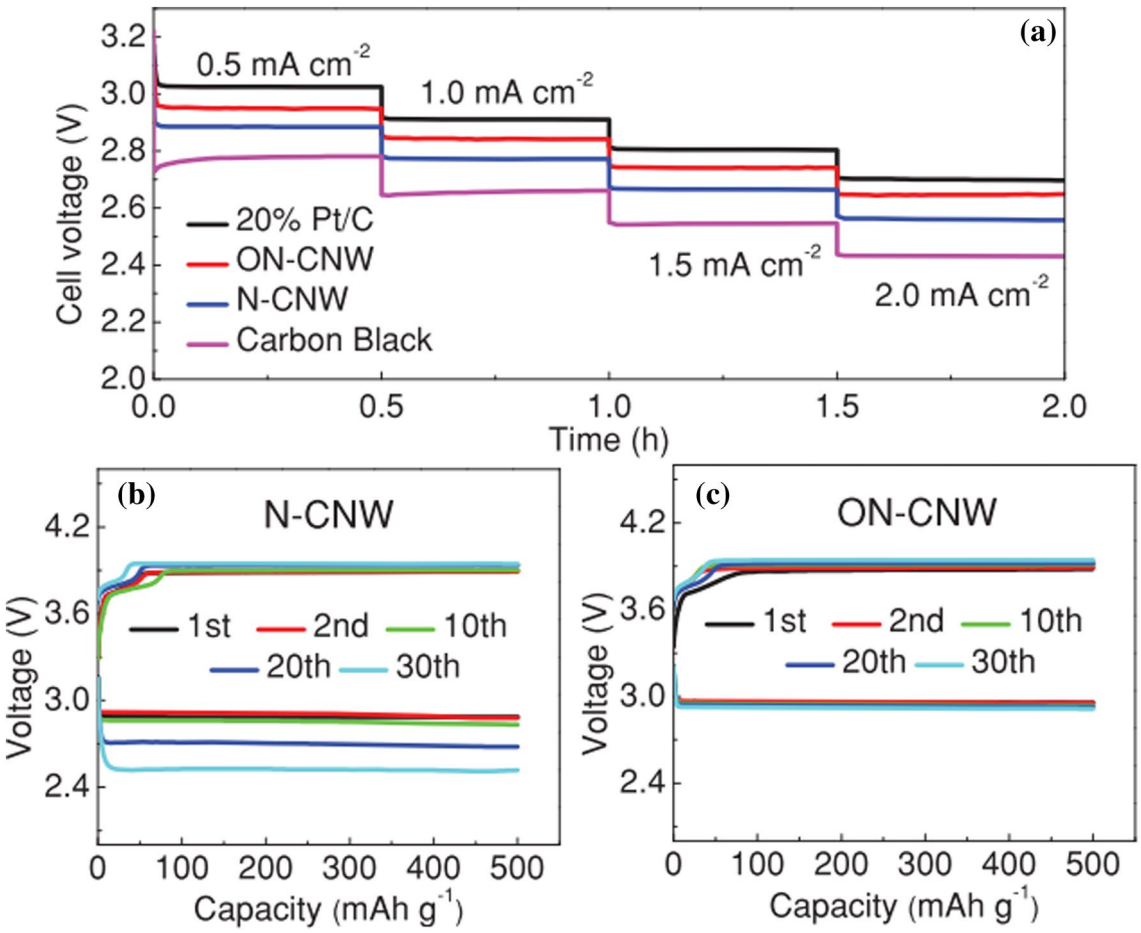

Fig. 4 **a** Discharge voltage profiles of hybrid LAB with Pt/C, N-CNW, ON-CNW, or carbon black as the ORR catalyst at different current densities. Cycling performance of hybrid LABs with **b** N-CNW or **c** ON-CNW as the ORR catalyst. Reprinted with permission from Ref. [23]. Copyright 2014 John Wiley and Sons

solutions. Interestingly, instead of 0.1 M KOH solution, an acidic medium (i.e., 0.5 M H_2SO_4 solution) was also used in the evaluation of the ORR performance of N-S-HPC. The obtained CV curves in O_2-saturated 0.5 M H_2SO_4 solution showed that N-S-HPC produced a slightly lower ORR activity than Pt/C as evidenced by the half-wave potential (~ 0.73 V) as compared with the half-wave potential (~ 0.78 V) of Pt/C. To demonstrate the potential of N-S-HPC catalysts in MABs, a ZAB with 6 M KOH was assembled for further electrochemical measurements using N-S-HPC as the air–cathode catalyst. The peak power density obtained using N-S-HPC was ~ 536 mW cm^{-2} and is drastically superior to Pt/C (~ 145 mW cm^{-2}). Therefore, the co-doping of N, S can result in an optimized combination of porous structures and surface functionalities for N and S and thus the enhancement of electrocatalytic activity.

Zhang et al. [69] carried out experiments in synthesizing and comparing three different co-doped carbon catalysts: N, S co-doped graphdiyne (NSGD), N, B co-doped graphdiyne (NBGD), and N, F co-doped graphdiyne (NFGD). After a series of electrochemical measurements in an assembled primary ZABs, the ORR activity of NFGD was found to be comparable to that of commercial Pt/C (20 wt% Pt on Vulcan XC-72) and superior to those of the other two dual-doped GDs. A first-principle study to theoretically demonstrate the synergistically enhanced catalytic effects of co-doping in B, P co-doped graphene was also carried out to compare with B-doped graphene and P-doped graphene [22].

4 Composites of Carbon and Metals

4.1 Composites of Carbon and Noble Metals or Noble Metal-Alloys

4.1.1 Composites of Carbon and Pt or Pt-Alloys

The composites of carbon and Pt have commonly been utilized as carbon-supported Pt fuel cell electrocatalysts for ORR in which different carbon materials act as high surface area substrates for the structuring and proper dispersion of Pt nanoparticles to form carbon-supported Pt-based catalysts. However, it has been well documented that Pt/C alone is not an efficient bifunctional electrocatalyst because of its insufficient OER performances [84–86]. To address the primary challenges of OER, metals such as Au [8, 87, 88], Co [89], Zn [90], Ir [7, 91], Pd [91], and Ru [91] have been used to form carbon-supported Pt-alloy catalysts in various metal–air batteries. Using the active effects of Au on the surface modification of Pt, Lu et al. [8] combined Au and Pt into individual PtAu nanoparticles on the surface of carbon and evaluated the ORR and OER activities of the resulting 40 wt% PtAu/C in LABs. In their study, $HAuCl_4$ and H_2PtCl_6 were used as Au and Pt sources to prepare 40 wt% PtAu/C and TEM images revealed a uniform distribution of PtAu nanoparticles [(~ 6.8 ± 1.4) nm] on carbon with XRD data (Fig. 5a), indicating a solid-solution composed of Pt and Au corresponding to $Pt_{0.5}Au_{0.5}$. From the CV curves (Fig. 5b) of the 40 wt% PtAu/C, the calculated electrochemical surface area (ESA) of the Pt and Au was (38 ± 4) $m^2\ g_{PtAu}^{-1}$ and correlated with the dispersion of PtAu observed in the TEM. In their investigation of ORR/OER using an assembled LAB, a comparison of first discharge and charge voltages (Fig. 5c) showed that the discharge voltage of 40 wt% PtAu/C is comparable to that of 40 wt% Au/C, and the charge voltage of 40 wt% PtAu/C is comparable to that of 40 wt% Pt/C. Moreover, 40 wt% PtAu/C as a cathode catalyst provided higher round-trip efficiencies than pure carbon even though both possessed similar specific capacities in the first cycle (~ 1200 mAh g_{carbon}^{-1}). This suggests that the incorporation of Au into Pt surfaces can result in improved ORR and OER kinetics of 40 wt% PtAu/C. However, at increasing charging cycles, the charge voltage of 40 wt% PtAu/C was lower than that of 40 wt% Pt/C and if current densities were decreased, discharge and charge voltages reduced considerably (Fig. 5d). This research crucially demonstrates that PtAu/C is responsible for both ORR and OER after the incorporation of Au into Pt atoms on the nanoparticle surface, providing a reasonable strategy to develop bifunctional catalysts for RMABs. To further understand the effects of Pt and Au on ORR and OER, a Pt–Au alloy nanoparticle catalyst supported on carbon black (Vulcan XC-72) [87] was found to played an important role in the charge/discharge performance of rechargeable LABs owing to their nanoscale alloying and phase properties inducing synergistic effects between the AuPt alloy and C.

Similar to Au, Co has also been used to form Pt–Co alloy nanoparticles supported on Vulcan XC-72 carbon in the application of LABs. To fabricate Pt_xCo_y/Vulcan XC-72 catalysts with a loading of 20 wt%, Su et al. [89] conducted a chemical reduction method to deposit a series of Pt_xCo_y (x:y = 4, 2, 1, and 0.5) alloy nanoparticles onto Vulcan XC-72 using $H_2PtCl_6{\cdot}6H_2O$ and $CoCl_2{\cdot}6H_2O$ as Pt and Co sources. XRD confirmed the complete incorporation of Co into the fcc crystal structure of Pt with an average crystallite size for all catalyst samples being in the range of 5–8 nm. This was also in agreement with TEM and HRTEM analysis. A combination of SEM and TEM showed that all Pt_xCo_y/C samples possessed carbon nanoparticles with similar morphologies in the size range of 50–100 nm and presented uniform distribution of Pt–Co alloy nanoparticles. In electrochemical performance tests in LABs, the discharge capacity of the $PtCo_2$/C cathode was found to have decreased from 2578 to 2074 mAh g^{-1} after 5 cycles, whereas the referenced Vulcan XC-72 cathode degraded from 965 to 376 mAh g^{-1}, demonstrating that $PtCo_2$/C possessed much better capacity

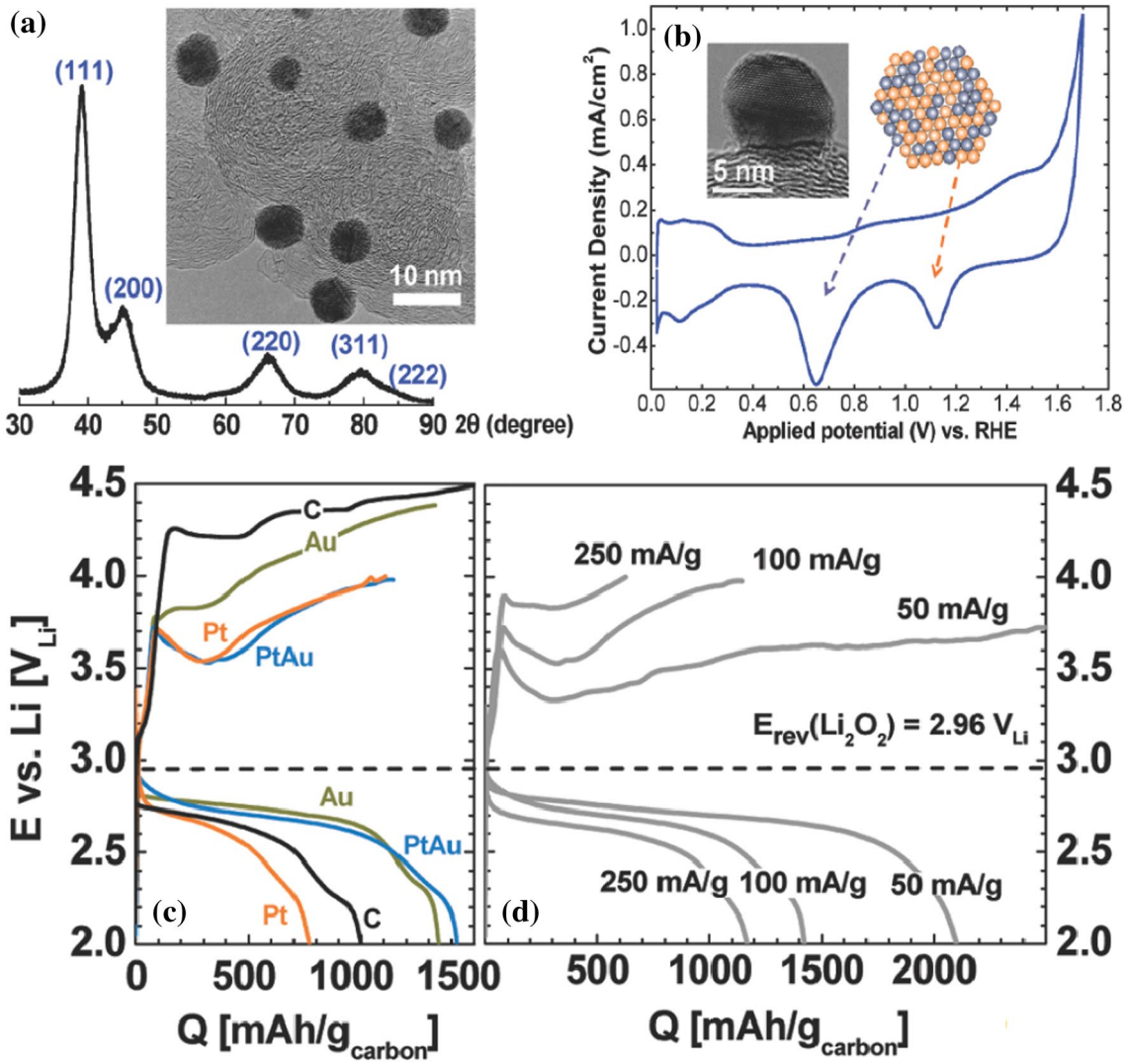

Fig. 5 **a** TEM image (top right) and XRD data of 40 wt% PtAu/C, **b** cyclic voltammograms of 40 wt% PtAu/C collected in Ar-saturated 0.5 M H_2SO_4 between 0.05 and 1.7 V versus RHE (room temperature and 50 mV/s). insets: (left) HRTEM image of 40 wt% PtAu/C and (right) schematic representation of Pt–Au, with arrows indicating the CV signatures for Pt (gray) and Au (yellow), **c** LAB first discharge/charge profile of carbon at 85 mA g^{-1}_{carbon} and of 40 wt% Au/C, 40 wt% Pt/C, and 40 wt% PtAu/C at 100 mA g^{-1}_{carbon}, **d** LAB discharge/charge profiles (first cycle) of 40 wt% PtAu/C at 50, 100, and 250 mA g^{-1}_{carbon}. Reprinted with permission from Ref. [8]. Copyright 2010 American Chemical Society

retention. Among all Pt_xCo_y/C samples, $PtCo_2$/C achieved a maximum capacity of 3040 mAh g^{-1}. This capacity was higher than that of the PtAu/C (1200 mAh g^{-1}) developed by Lu et al. [8]. This indicates that compared with Au, Co should be more suitable in Pt-alloys for the improvement of both ORR and OER. In further analyses of discharge and charge curves in the second cycle, Pt_xCo_y/C samples possessed much lower charge voltages (~ 3.94 V) and overpotentials (~ 1.21 V) than Vulcan XC-72 with specific capacities increasing positively with increasing Co content, indicating improved catalytic activities toward ORR and OER in LABs. Along with increasing Co content near Pt atoms, surface Pt electron density and segregation also increased, leading to enhancements in both OER and ORR activities. Cycling tests in LABs also confirmed better cyclability performances with Pt_xCo_y/C as compared with bare Vulcan XC-72. To further understand and obtain high ORR and OER activities from Pt-alloys with non-noble metals, Zhang et al. [90] synthesized PtZn/carbon aerogel alloy catalysts and measured the electrochemical performance of these catalysts (PtCo/carbon aerogel, Pt/carbon aerogel and Pt/carbon black) in magnesium–air batteries. In their study, the PtZn/carbon aerogel demonstrated a higher specific discharge capacity (1349.5 mAh g^{-1}) than the PtCo/carbon aerogel (~ 1283.38 mAh g^{-1}), Pt/carbon aerogel (~ 1113.53 mAh g^{-1}), and Pt/carbon black (~ 997.01 mAh

g^{-1}) catalysts, suggesting that PtZn/carbon aerogel possessed better ORR and OER activities.

As a noble metal, iridium also was used to alloy with Pt to prepare carbon-supported Pt–Ir catalysts for rechargeable LABs by Ke et al. [92], in which $H_2PtCl_6{\cdot}H_2O$ and $IrCl_3$ were used as Pt and Ir sources. In a comparison of OER, current–potential curves tested in a Ar-saturated 0.1 M KOH solution revealed that Pt/C provided a higher onset potential (~ 0.66 V) than Pt–Ir/C (~ 0.53 V) and Ir/C (~ 0.50 V) catalysts, indicating that Pt–Ir/C possessed better OER. For a comparison of first cycle discharge–charge potential profiles in discharge–charge measurements run in a LAB, Pt–Ir/C demonstrated the least discharge overpotential (~ 0.15 V) during the discharge process whereas at the end of the charging process, Pt–Ir/C possessed the lowest potential difference (~ 0.727 V) between the discharge and charge potentials. Therefore, Pt–Ir/C clearly exhibits enhanced ORR and OER.

4.1.2 Composites of Carbon and Other Noble Metals or Alloys

Aside from Pt and Pt-alloys, other noble metals (Ir, Ru, Pd, Au and Ag) and alloys have also been used to prepare noble metal-based electrocatalysts supported on carbon materials for MABs. Using Ir as a catalytic noble metal to functionalize catalytic surfaces of carbon, Zhou et al. [93] introduced nano-sized iridium (Ir) catalysts into a three-dimensional porous graphene for LABs using a non-aqueous electrolyte in which iridium functionalized deoxygenated hierarchical graphene (Ir@DHG) was synthesized using a vacuum-promoted exfoliation method followed by a deoxygenation process. The Ir@DHG was tested to possess a high BET surface area (~ 372.5 m^2 g^{-1}) and its nitrogen adsorption–desorption curves showed pore sizes ranging from 2 to 200 nm, indicating the presence of a fertile mesoporous and macroporous architecture favoring the transport of oxygen, electrolytes and electrons to and from catalytic sites during discharge and charge. According to XPS results, the Ir@DHG catalyst displayed smaller peaks for C1*s*. This is possibly because Ir can closely cover graphene and decrease the exposure of carbon surfaces. Importantly, Ir@DHG possessed a slightly lower intensity for O1*s* than DHG, suggesting that the graphene in Ir@DHG can maintain a highly deoxygenated surface and enhance the stability of the electrode/electrolyte interface [94, 95]. The high-resolution XPS spectrum of Ir 4*f* presented dominating Ir(0) $4f_{5/2}$ and Ir(0) $4f_{7/2}$ with factional Ir(IV) $4f_{5/2}$ and Ir(IV) $4f_{7/2}$. This suggests a certain degree of surface oxidation. TEM showed the uniform distribution of Ir nanoparticles (~ 2.08 nm) onto the entire graphene plane and CV tests in LABs at 1 mV s^{-1} showed that Ir@DHG possessed higher current peaks, indicating better ORR activity than DHG. Two large oxidation peaks at 3.25 and 4.37 V of Ir@DHG also indicated much higher anodic currents. These results illustrated that Ir@DHG possesses superior OER activity compared with DHG. Cycling performances at a current density of 2000 mA g^{-1} with a limited capacity of 1000 mAh g^{-1} revealed that Ir@DHG can run 150 cycles with terminal voltages greater than 2.5 V, demonstrating that Ir@DHG also possessed better reversibility and cycling performance than DHG.

Ruthenium (Ru) [96, 97] and palladium (Pd) [98–100] have also been used to functionalize carbon to reduce overpotentials and capacity decays during round-trip cycling in rechargeable LABs. Using a type of carbonized bacterial cellulose (CBC) as a carbon support, Tong et al. [96] prepared a 5 wt% Ru/CBC composite as the binder-free cathode in non-aqueous LABs in which Ru nanoparticles can provide active sites for both ORR and OER, and CBC can provide transport pathways for both electrons and oxygen. Both BET and TEM measurements showed a high surface area of 397.6 m^2 g^{-1} and a porous network structure for the 5 wt% Ru/CBC catalyst, favoring the distribution of active sites and mass transport. The obtained galvanostatic discharge-recharge curves at a current density of 200 mA g^{-1} displayed a narrower discharge–charge potential gap than that of CBC, indicating that 5wt% Ru/CBC possessed better ORR and OER activities. Corresponding SEM images of 5wt% Ru/CBC after charging showed uniform deposition of discharge products (i.e., Li_2O_2) on the CBC surface, demonstrating the strong interaction between Li_2O_2 and CBC and the improvement of stability of the tested LAB with 5 wt% Ru/CBC. Similar to Ru functionalized CBC catalysts, Pd-catalyzed carbon nanofibers (Pd/CNF) catalysts were also prepared for alkaline MABs by Alegre et al. [98] in which a commercial Vulcan carbon was employed as a reference support material to support Pd nanoparticles. Characterization by XRD, TEM, and SEM showed that the Pd/CNF and Pd/Vulcan catalysts possessed typical fcc structures of Pd and the calculated crystallite sizes of the Pd/CNF and Pd/Vulcan catalysts were 6.1 and 6.5 nm, respectively. In the examination of ORR and OER in a half-cell configuration, two full polarization curves obtained from 1.2 to 0.3 V under ORR and from 1.2 to 2.0 V under OER showed that Pd/CNF possessed slightly smaller overpotentials than Pd/Vulcan and was therefore slightly more active. This was possibly attributed to the higher electrical conductivity and/or smaller Pd size of Pd/CNF, favoring better charge transfers and thus improved ORR and OER. Further charge/discharge cycle tests showed that Pd/CNF could run more cycles than Pd/Vulcan and was therefore more stable as well. Au [101] and Ag [102] were also used to functionalize carbon materials in the application of MABs. A recent study [97] of Ru- and Pd-catalyzed carbon nanotube fabrics showed that Ru- and Pd-CNT catalyzed cathodes for LABs do not show visible

improvements. This is possibly because the presence of noble metal catalysts impairs the reversibility of cells, causing a decrease in O_2 recovery efficiency (the ratio between the amount of O_2 evolved during charge and the amount consumed in the preceding discharge) coupled with an increase in CO_2 evolution during charging.

Because carbon-supported Pt-based binary metal catalysts exhibit active ORR and OER activities for enhanced LAB performance, carbon-supported non-platinum binary metal catalysts such as Pd_3Pb/C [103] and PdIr/C [91] have also been studied for carbon-composited bifunctional catalysts in MABs. To replace expensive Pt-based alloy catalysts, Cui et al. [103] synthesized a Pd_3Pb/C catalyst using a modified impregnation-reduction method in which they carefully controlled the experimental conditions (e.g., temperature, time, reduction agent, metal precursor) to obtain a structurally ordered intermetallic phase that provided uniform active sites on the same surface plane. In characterizations, XRD confirmed the ordered Pd_3Pb/C structure and TEM images showed that Pd_3Pb/C possessed a uniform particle distribution with an average particle size of (7.2 ± 0.5) nm. The particle sizes of the Pd/C and Pt/C catalysts were (6.3 ± 0.4) and (5.1 ± 0.3) nm, respectively. Polarization curves in O_2-saturated 0.1 M KOH solution at 1600 r min^{-1} revealed that Pd_3Pb/C was more active than both Pd/C and Pt/C catalysts, evidenced by a more positive onset potential and a greater half-wave potential (~ 0.92 V) than Pd/C (~ 0.88 V) and Pt/C (~ 0.88 V) catalysts. Importantly, after the incorporation of Pd, Pd_3Pb/C gained better catalytic activities toward ORR and OER and possessed better durability than Pt/C. This was confirmed in the measured discharge and charge voltage profiles of an assembled ZAB using Pd_3Pb/C as the cathode catalyst, in which initial round-trip overpotentials increased from 0.72 V at the first cycle to 0.86 V at the 135th cycle. Besides Pd_3Pb/C catalysts, PdIr/C was also studied by Ko et al. [91]. Based on initial charge–discharge behaviors, a comparison of ORR and OER showed that PtRu/C possessed lower overpotentials for charging and discharging than PtPd/C and PtIr/C, in which the capacity followed an order: PtRu/C (~ 346 mAh g^{-1}) > PtPd/C (~ 153 mAh g^{-1}) > PdIr/C (~ 135 mAh g^{-1}). Table 2 shows the electrochemical performances for typical noble metal–carbon composite bifunctional catalysts as cathodes in MABs [86, 87, 89, 91, 92, 96, 100, 104].

To improve the ORR and OER (especially OER) of Pt/C catalysts, the incorporation of other metals can play an important role in improving battery performance in rechargeable MABs due to the synergistic interactions between different components. For example, composite catalysts such as $PtCo_2/C$ [89] and Pt/CNTs/Ni [104] can deliver high discharge capacities of 3040 and 4050 mAh g^{-1} for MABs, respectively. Compared to pure Pt catalysts, other noble metals (e.g., Ir or Ru) are also able to increase OER favoring cycling performances. The incorporation of transitional non-noble metals such as Co and Ni can also improve the cycle life of MABs, as evidenced in Table 2. And although noble metal-based bifunctional catalysts incorporated by other noble metal component(s) can play an important role in improving the bifunctional activity and stability of ORR/OER, their high price and scarcity present barriers for scale-up deployment in MAB commercialization.

4.2 Composites of Carbon and Non-noble Metals

Non-noble metals have been incorporated into carbon materials to enhance both ORR and OER, reduce carbon corrosion, and improve reversibility and rate capabilities of carbon-composited bifunctional catalysts for MABs. These materials are inexpensive, easily fabricated, and possess good interactions with carbon. For example, tantalum (Ta) was found to reduce battery polarization and overpotential by Yu et al. [105] in which they developed vertically aligned CNTs (VACNTs) with ultra-lengths on permeable Ta foils (VACNTs-Ta) as air cathodes for non-aqueous secondary LABs using a thermal chemical vapor deposition (TCVD) method. In their study, CNT powder (CNT-P, 20–40 μm in length and 15 nm in outer diameter) and commercial VACNT on a stainless steel (SS) mesh substrate (VACNTs-SS) were used as the reference samples. Compared with the VACNTs-SS and CNT-P samples, VACNTs-Ta presented a lower ratio of D band and G band as observed by Raman spectroscopy, demonstrating that VACNTs-Ta possessed less surface defects and lower reactivity with O_2 reduction species. The combination of BET and BJH revealed the coexistence of micropores, mesopores, and macropores in the VACNTs-Ta in which mesopores and macropores were the majority, favoring the transport of mass and thus improving catalytically properties. In the comparison of electrochemical properties, the first discharge and charge behaviors of an assembled LAB showed that as a cathode, VACNTs-Ta can deliver a larger gravimetric specific capacity (~ 4300 mAh g^{-1}) at 200 mA g^{-1} than VACNTs-SS (~ 3200 mAh g^{-1}) and CNT-P (~ 700 mAh g^{-1}). These results confirmed that VACNTs-Ta possessed greater ORR and OER activities than the other two samples. In further tests of cycling and rate capability, VACNTs-Ta also exhibited better cycling performances (65 cycles at 200 mA g^{-1} as well as a curtailed specific capacity of 1000 mAh g^{-1}) and rate capabilities (10,000 mAh g^{-1} at 50 mA g^{-1}), suggesting that VACNT-Ta possessed more a favorable architecture and higher stability than those of the VACNT-SS and CNT-P samples. The researchers concluded that the use of Ta not only favored the fabrication of VACNT but also produced beneficial interactions between Ta and VACNT, benefiting co-transportation/reaction and thus the reduction of discharge product (e.g., Li_2O_2) aggregation. To further develop high-performance

Table 2 Electrochemical performance for typical noble metal-based bifunctional catalysts as air-electrode materials in the tested MABs

No.	Bifunctional catalyst as cathode materials	Maximum capacity/mAh g^{-1} (current density/[a]mA g^{-1} or [b]mA cm^{-2})	Cycle number (current density/ mA g^{-1} or mA cm^{-2}, upper-limit capacity/ mAh g^{-1})	Potential range for cycle testing (V)	Potential difference for ORR/OER (initial ORR/OER overpotentials[c], V vs. Li/Li^+)	Coulombic efficiency (%, after cycle number)	Electrolyte type	MAB type	References
1	10 wt% Pt/GNS	1200 (70[a])	20 (100[a], 720)	2.0–4.8	0.97 (2.88/3.85)	–	1 M $LiPF_6$ in EC:DMC[d] (1:1 v/v)	LAB	[86]
2	20 wt% $Pt_{51}Au_{49}$/C	1329 (0.12[b])	1 (0.12[b], 240)	2.0–4.5	1.30 (2.70/4.00)	–	1 M $LiPF_6$ in EC:DMC[d] (1:1 v/v)	LOB	[87]
3	20 wt% $PtCo_2$/C	3040 (100[a])	5 (100[a], –)	2.0–4.6	1.21 (2.73/3.94)	–	1 M $LiClO_4$ in PC:DME[e] (1:2 v/v)	LAB	[89]
4	44 wt% $Pt_{50}Ru_{50}$/C	700 (0.2[b])	40 (0.2[b], 700)	2.3–4.5	1.20 (2.66/3.86)	–	1 M $LiPF_6$ in TEGDME	LAB	[91]
5	36.5 wt% Ir@DHG	–	150 (2000[a], 1000)	1.5–4.5	1.07 (2.74/3.81)	–	0.1 M $LiClO_4$ in TEGDME:DMSO (1:2 v/v)	rLOB	[93]
6	5 wt% Ru/CBC	–	25 (200[a], 500)	2.0–4.5	1.26 (2.71/3.97)	–	$LiCF_3SO_3$:TEGDME (4:1 mol/mol)	LOB	[96]
7	40.12 wt% Pt/C	616 (70[a])	10 (70[a], –)	2.0–4.3	0.83 (2.72/3.55)	–	1 M $LiPF_6$ in PC	rLAB	[100]
	40.03 wt% Pd/C	855 (70[a])	10 (70[a], –)		0.75 (2.65/3.40)	–			
	40.15 wt% Ru/C	577 (70[a])	10 (70[a], –)		0.84 (2.76/3.70)	–			
8	Pt/CNTs/Ni	4050 (20[a])	80 (400[a], 1500)	2.0–4.2	1.10 (2.60/3.70)	–	1 M LITFSI in TEGDME	LOB	[104]

[a]mA g^{-1}

[b]mA cm^{-2}

[c]Initial overpotentials are obtained from the cyclic tests

[d]Dimethyl carbonate

[e]1,2-Dimethoxyethane

non-noble metal-functionalized carbon cathode materials, Su et al. [106] studied the composites of carbon with Ni, Co, and Cu quantum dots (QDs) and compared them with a MnO/carbon composite. Based on capacitance and rate performance results, the researchers demonstrated that Ni, Co, and Cu QDs composited with carbon is an important path in developing advanced carbon-based cathode materials in LABs.

Although single non-noble metals have been explored for novel carbon-based composites, research has also been carried out using two non-noble metals (e.g., transition metals such as Co, Ni, Fe, Cu, and Mn) in carbon-composited catalysts for MABs in which stronger synergistic effects between the two metals and carbon are expected. To hinder the restacking of graphene layers and increase the space between layers favorable to the transport of oxygen, lithium ions and electrolyte, Chen et al. [107] designed and synthesized cost-effective cobalt-copper bimetallic yolk-shelled nanoparticles supported on graphene (CoCu/graphene) as a composite cathode catalyst for LABs. XRD confirmed the coexistence of Co and Cu along with graphene, and TEM images revealed highly distributed CoCu nanoparticles with an average diameter of 10–20 nm on graphene sheets without aggregation, meaning that more active sites were formed. The electrocatalytic activity measurements in the first discharge–charge profiles of their LAB with a voltage range of 2.0–4.3 V at 200 mA g^{-1} showed larger discharge capacities (14,821 mAh g^{-1}) and coulombic efficiencies (92%) than compared with Co/graphene and Cu/graphene cathodes, indicating that CoCu/graphene possessed better electrocatalytic activity. Moreover, Co/graphene presented much higher coulombic efficiencies than Cu/graphene, demonstrating that Co can efficiently accelerate OER and that Cu can have a positive influence on ORR. In a comparison of CV curves, CoCu/graphene exhibited the most positive ORR onset potential and the greatest ORR/OER

peak current density, confirming the higher catalytic activity of CoCu/graphene as compared with Co/graphene and Cu/graphene cathodes. In cycling tests performed in a LAB with a current density of 200 mA g^{-1} and a cutoff capacity of 1000 mAh g^{-1}, the discharge voltages of Co/graphene and Cu/graphene cathodes degraded to less than 2.5 V after only 71 and 37 cycles, respectively, whereas CoCu/graphene remained above 2.5 V for 122 cycles, once again demonstrating the superior ORR stability of CoCu/graphene. This cycling test was subsequently extended to a higher current density of 500 mAh g^{-1} with a cutoff capacity of 1000 mAh g^{-1}, and the CoCu/graphene run stably for 204 cycles with a discharge terminal voltage of 2.0 V. This was better than Co/graphene (~ 144 cycles) or Cu/graphene (~ 101 cycles). The cycling performance of CoCu/graphene was shown to be comparable to those of the best cycling performances in LABs [108, 109]. A similar study was conducted by Kwak et al. [110], in which CNT was composited with Fe and Co as a cathode catalyst for LABs. In their characterization using SEM, TEM, XRD, EDS, and SAED patterns, bimetallic Fe and Co coupled with a small amount of oxidized states, were confirmed in the FeCo–CNTs catalyst (Fig. 6). In an assembled LAB, the FeCo–CNT cathode demonstrated greater capacity (~ 3600 vs. ~ 1276 mAh g^{-1}) and better round-trip efficiency (72.15 vs. 62.5%) than pristine CNTs, indicating that FeCo–CNTs possessed superior ORR and OER activities.

Besides the CoCu/graphene and FeCo–CNTs composite catalysts discussed above, electrospun graphitic carbon nanofibers with in situ encapsulated Co–Ni nanoparticles (Co–Ni/CNFs) were also developed by Huang et al. [111], in which the encapsulation of metal catalysts into nanocarbon can suppress aggregation, presenting more active sites for both ORR and OER. In their synthesis, cobalt(II) acetate terahydrate ($Co(Ac)_2{\cdot}4H_2O$) and nickel(II) acetate tetrahydrate ($Ni(Ac)_2{\cdot}4H_2O$) were used as Co and Ni sources. In their examination of electrocatalytic activity using an assembled non-aqueous LAB without any binders or additives, a cyclic test with an upper-limit capacity of 1000 mAh g^{-1} at 200 mA g^{-1} showed that the Co–Ni/CNFs cathode can run 60 cycles with initial overpotentials of only 0.22 and 0.70 V for ORR and OER, respectively. Importantly, in the first discharge/charge curves obtained at 200 mA g^{-1}, Co–Ni/CNFs displayed an initial discharge capacity of 8635 mAh g^{-1}. This was better than that of CNFs, suggesting that the in situ formation of Co–Ni improved electrochemical performances and enhanced ORR and OER. Their results showed that the inherently interconnected, conductive network of Co–Ni/CNFs is sufficient for LABs without any binders and additives. Ren et al. [112] found that CuFe catalyzed carbon black (Ketjenblack) materials can drastically increase the density of catalytic sites, resulting in improvements of LAB ORR kinetics.

As listed in Table 3 [105, 107, 110, 111, 113–119], instead of high-priced noble metals, the use of non-noble metals in bifunctional composite catalysts can generally improve MAB performances because of the formation of various decent structures and the synergistic effects between different components. For example, at 200 mA g^{-1}, CoCu/grapheme [107] can deliver high discharge capacities of over 100,000 mAh g^{-1} as well as acceptable cycle performances (i.e., cycle number above 70). Interestingly, based on non-noble metal and carbon, ternary and quaternary composite catalysts, such as Fe–Fe_3C/CNFs [113], $FeNi_3$@GR@Fe–NiOOH [114], Co_3O_4/Ni/C [119], and Co/C/NiFe LDH/AB [113] have demonstrated even better activities toward ORR and OER, resulting in enhanced MAB performances in terms of capacity, cycling stability and/or energy efficiency. In addition, by comparing non-noble metal-based with noble metal-based bifunctional catalysts as shown in Table 3, it can be seen that in terms of tested cycle numbers, non-noble metal-based catalysts can achieve almost better cycling performances in MABs than noble metal-based catalysts, as shown in Table 2. Non-noble metals can also provide acceptable bifunctionality resulting from its formed nanostructures as well as its strong interactions with supporting materials (like carbons).

In the search for next-generation bifunctional catalysts for scale-up deployment in MAB commercialization, non-noble metal-based catalysts are more promising than noble metals. Not only are non-noble metals cheaper and more abundant than noble metals, non-noble metals can easily be fabricated with supporting materials (e.g., carbon) in the formation of efficient nanostructures to improve bifunctional activities and stability by building important interactions with the supporting material.

5 Composites of Carbon and Oxides

In recent years, metal oxides have been reported to exhibit promising activities for ORR and OER. However, the self-passivity and low electrical conductivity of metal oxides can decrease active sites and hinder charge transport, leading to low catalytic performances [120, 121]. Therefore, compositing conductive carbon and oxides have become an effective strategy to enhance catalytic performances because these composites can overcome these low conductivity and corrosion drawbacks [122, 123].

5.1 Composites of Carbon and Perovskite Oxides

Perovskite oxides, with a general formula of ABO_3 [124] (Fig. 7, the A-site is a rare alkaline earth metal cation and the B-site is a 3*d* transition metal cation), have attracted increasing attention because of their defective structures,

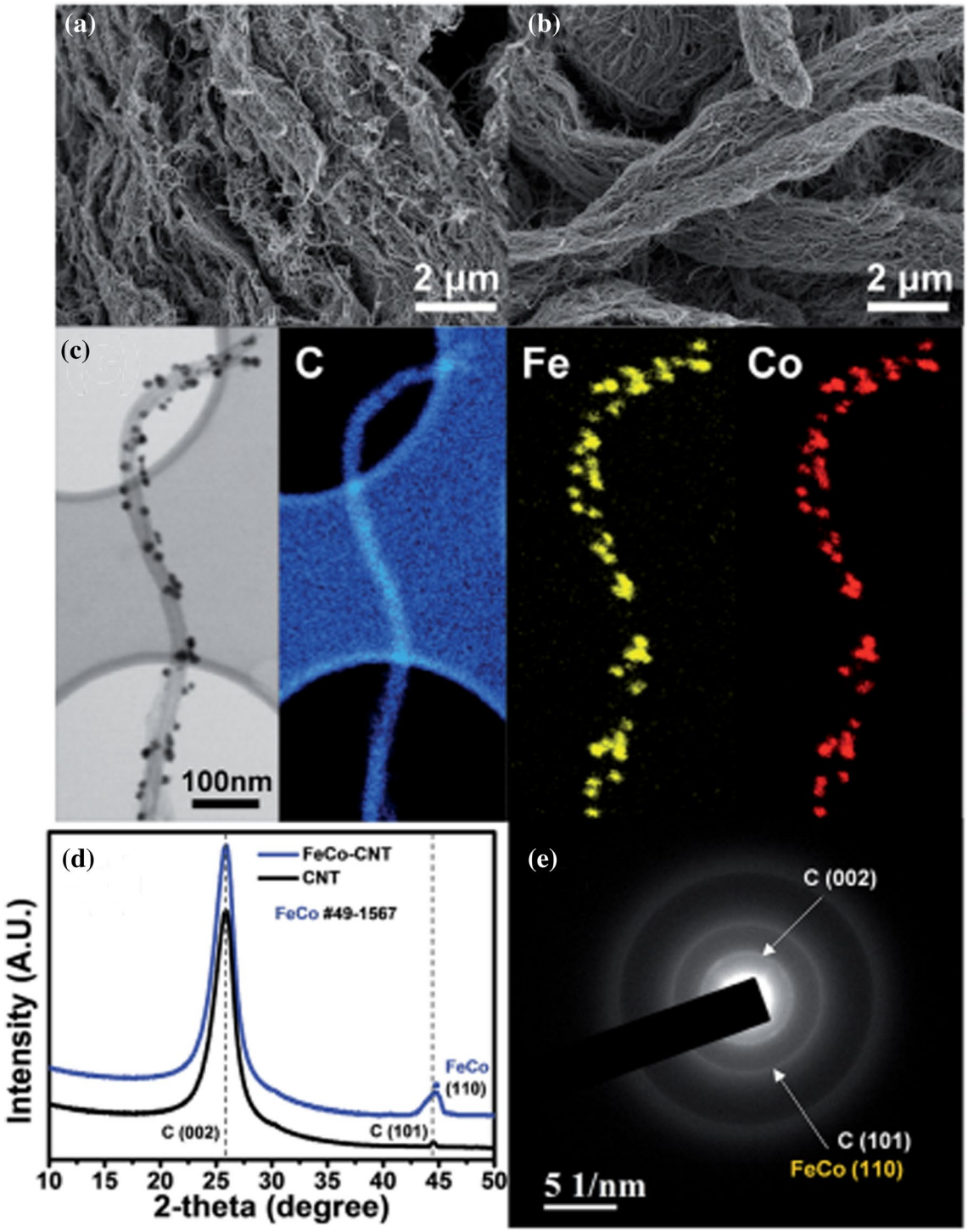

Fig. 6 Morphology and structure of the synthesized FeCo–CNTs composite. SEM images of **a** FeCo–CNTs and **b** pristine CNTs; **c** TEM image of FeCo–CNTs with EDS mapping images; **d** XRD patterns of FeCo–CNTs and pristine CNTs. **e** SAED patterns of FeCo–CNTs. Reprinted with permission from Ref. [110]. Copyright 2016 Royal Society of Chemistry

low costs, excellent oxygen mobility, and outstanding activities toward ORR and OER [125, 126]. To improve overall energy efficiency and retain stability, perovskite oxides have been proposed to composite with carbon to improve ORR and OER activities in alkaline environments owing to three aspects: the active oxide, the conductive carbon support, and the synergistic effects between them.

Table 3 Electrochemical performance for typical non-noble metal-based bifunctional catalysts as air-electrode materials in the tested MABs

No.	Bifunctional catalyst as cathode materials	Maximum capacity/mAh g^{-1} (current density/[a]mA g^{-1} or [b]mA cm^{-2})	Cycle number (current density/mA g^{-1} or mA cm^{-2}, upper-limit capacity/mAh g^{-1})	Potential range for cycle testing (V)	Potential difference for ORR/OER (initial ORR/OER overpotentials[c], V vs. Li/Li^+)	Energy efficiency (%)	Electrolyte type	MAB type	References
1	Ta/CNTs	4300 (200[a])	65 (200[a], 1000)	2.0–4.5	1.70 (2.60/4.30)	–	1 M LiTFSI/TEGDME	rLOB	[105]
2	CoCu/graphene	14,821 (200[a])	122 (200[a], 1000)	2.5–4.5	1.05 (2.75/3.80)	–	1 M LiTFSI/TEGDME	rLOB	[107]
3	FeCo/CNTs	3600 (250[a])	50 (100[a], 1000)	2.4–4.5	1.14 (2.75/3.89)	–	1 M LiTFSI/TEGDME	rLOB	[110]
4	CoNi/CNFs	8635 (200[a])	60 (200[a], 1000)	2.0–4.5	0.92 (–/–)	–	0.5 M LiTFSI/TEGDME	rLOB	[111]
5	Fe–Fe_3C/CNFs	6250 (200[a])	41 (300[a], 600)	2.0–4.3	1.05 (2.70/3.75)	–	1 M LiTFSI/TEGDME	rLOB	[113]
6	$FeNi_3$@GR@Fe–NiOOH	–	100 (1[b], –)	0.9–2.1	0.90 (1.05/1.95)	–	6 M KOH	rZAB	[114]
7	Co/C/NiFe LDH/AB	–	300 (40[b], –)	1.05–2.05	0.75 (1.20/1.95)	51.2%	6 M KOH	rZAB	[115]
8	Co–N/C	–	500 (2[b], –)	0.4–1.4	0.94 (1.21/2.15)	–	6 M KOH	ZAB	[116]
9	Fe–N/C	731 (100[b])	–	–	–	–	6 M KOH	ZAB	[117]
10	Fe@N–C	–	100 (10[b], –)	1.0–2.0	0.70 (1.25/1.95)	–	6 M KOH	ZAB	[118]
11	Co_3O_4/Ni/C	14,830 (400[a])	48 (100[a], 2000)	2.0–4.3	0.55 (2.69/3.24)	75.1%	0.1 M $LiClO_4$/DME	LOB	[119]

[a]mA g^{-1}

[b]mA cm^{-2}

[c]Initial overpotentials are obtained from the cyclic tests

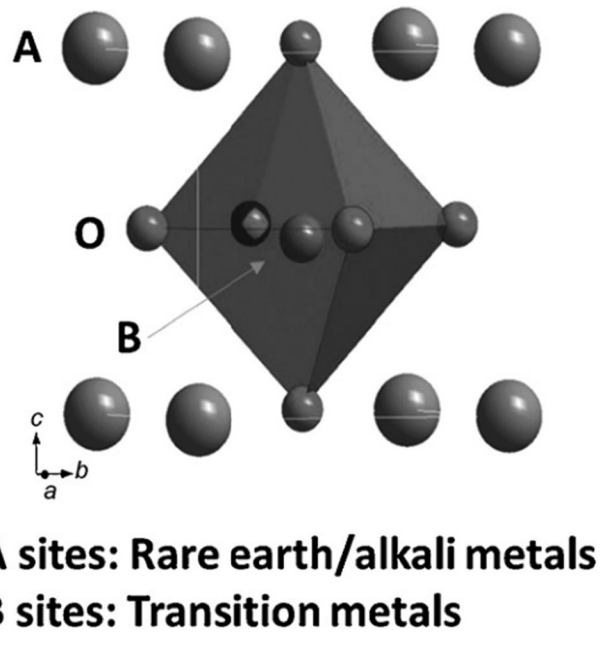

Fig. 7 A unit cell in perovskite showing the relative positions of different ions. Reprinted with permission from Ref. [124]. Copyright 2016 John Wiley and Sons

To enhance the electrical conduction of perovskite oxides and investigate the effects of perovskite oxides on ORR and OER, Xu et al. [127] studied $BaMnO_3$–carbon composites and their bifunctional electrocatalytic capabilities for ORR and OER. Their carbon-coated $BaMnO_3$ nanorod ($BaMnO_3$@5%C) samples were synthesized through a coating method in which $BaCl_2$ and MnO_2 were used as Ba and Mn sources with a ratio of Ba to Mn being 1:1. SEM images of the product revealed $BaMnO_3$ nanorods 100–200 nm in diameter and 1–4 μm in length and TEM revealed that these nanorods were compactly and uniformly coated with a 10-nm-thick carbon. The comparison of $BaMnO_3$ with $BaMnO_3$@5%C samples by XRD evidenced the presence of perovskite $BaMnO_3$ structures with a small amount of MnO_2 resulting from residual raw reactants. In the investigation for ORR and OER, CV curves in O_2-saturated 0.1 M KOH solution showed that the peak current density (~ 2.5 mA cm^{-2}) of $BaMnO_3$@5%C was much greater than that of $BaMnO_3$ (~ 0.94 mA cm^{-2}), demonstrating superior electrocatalytic activity. This result was further confirmed by tested LSV curves in which $BaMnO_3$@5%C possessed a larger positive half-wave potential as compared with $BaMnO_3$. Moreover,

the diffusion limiting current density of $BaMnO_3$@5%C was comparable to commercial Pt/C (20wt% Pt on Vulcan XC-72) catalysts. Interestingly, $BaMnO_3$@5%C possessed an ORR electron transfer number of ~ 3.8. This was higher than that of $BaMnO_3$ (3.4 – 3.7) and close to that of Pt/C (~ 3.9). $BaMnO_3$@5%C also demonstrated better OER activity because it exhibited greater current densities and more negative onset potentials than $BaMnO_3$ and Pt/C as revealed by linear scanning voltammograms in N_2-saturated 0.1 M KOH solution at a rotation speed of 1600 r min^{-1}. In terms of stability, durability tests were run for ORR and OER using a chronoamperometric method for 12 h in O_2- and N_2-saturated 0.1 M KOH at 1600 r min^{-1}. Here, $BaMnO_3$@5%C provided better stability toward ORR and OER compared with both Pt/C and $BaMnO_3$ samples. Not all carbon materials enhance ORR and OER after compositing with perovskite oxides, however. For example, $LaMnO_3$-C exhibited poor OER activity after the incorporation of carbon [128].

For perovskite oxides with the general formula of ABO_3, the substitution of the A-site and/or B-site metal cations to generate oxygen deficiency/vacancy can have large characteristic effects on their electronic structure and coordination chemistry, leading to enhanced ORR and OER activities [129]. Two typical representatives of perovskite oxides with a partial A-site substitution, $La_{0.6}Ca_{0.4}CoO_3$ (LCC) and $Sr_{0.5}Sm_{0.5}CoO_{3-\delta}$ (SSC) have been combined with carbon black to form two different carbon-supported perovskite oxides (C-LCC and C-SSC) for rechargeable MABs [11, 130]. In a comparison of their bifunctionality using graphitized Vulcan XC-72R as a reference, obtained cathodic polarization curves in a three-electrode cell with an 8.5 M KOH solution revealed that the C-SSC composite cathode provided better ORR activities that the C-LCC cathode and both cathodes exhibited better ORR activities than the graphitized Vulcan XC-72R cathode. No significant difference in OER activity was found between the C-SSC and C-LCC cathodes, however, but both still provided better OER activities than the graphitized Vulcan XC-72R cathode. In cycling performance tests under 53 mA cm^{-2}, C-SSC ran for 106 cycles at − 0.3 V, whereas C-LCC only ran for ~ 68 cycles at − 0.3 V. The graphitized Vulcan XC-72R exhibited unsatisfactory cycling performances because of its poor OER capabilities. Later, Velraj and Zhu [11] also prepared untreated Vulcan XC-72R supported LCC and SSC and their results showed that because of the better corrosion resistance of graphitized carbon, graphitized Vulcan-based electrodes can provide more than twice the cycle life of untreated carbon-based electrodes. These results confirm that for carbon-supported perovskite oxide composites, the enhancement of catalytic activity and durability toward ORR and OER are related to the structure and properties of the carbon and perovskite oxides, as well as the synergistic effects between them.

In addition to the partial substitution of A-sites, the partial substitution of B sites was also successfully conducted to form new perovskite oxides for MAB carbon-composited catalysts. Yuasa et al. [131] prepared carbon-supported $LaMn_{0.6}Fe_{0.4}O_3$ (C-$LaMn_{0.6}Fe_{0.4}O_3$) electrocatalysts using a reverse homogeneous precipitation (RHP) method and investigated the effects of $LaMn_{0.6}Fe_{0.4}O_3$ on discharge and charge properties in LABs. XRD revealed that the obtained C-$LaMn_{0.6}Fe_{0.4}O_3$ was in a perovskite-phase of an orthorhombic form without any other impurity phases with a calculated crystalline size of 17.4 nm. TEM images showed the uniform distribution of $LaMn_{0.6}Fe_{0.4}O_3$ on carbon. The size range of $LaMn_{0.6}Fe_{0.4}O_3$ was 15–20 nm, and this was consistent with XRD results. Used in an LAB, the obtained four charge/discharge curves at 0.5 mA cm^{-2} showed that as compared with C-$LaMn_{0.6}Fe_{0.4}O_3$, carbon presented an unstable charge voltage due to its oxidation corrosion by anodic polarization [132]. With the addition of $LaMn_{0.6}Fe_{0.4}O_3$, C-$LaMn_{0.6}Fe_{0.4}O_3$ exhibited stable discharge/charge curves because $LaMn_{0.6}Fe_{0.4}O_3$, with a higher OER, effectively prevents oxidation corrosion from anodic polarization. The discharge voltages of the C-$LaMn_{0.6}Fe_{0.4}O_3$ were also greater than that of carbon, suggesting that $LaMn_{0.6}Fe_{0.4}O_3$ can also act as an ORR catalyst in non-aqueous electrolytes as well as in alkaline aqueous solutions because Mn^{3+} or Mn^{4+} ions can act as active sites for ORR [133]. Researchers [134, 135] have also studied carbon-composited perovskite oxides derived from the substitution of both A and B sites as oxygen electrodes and have also found improved electrochemical properties.

5.2 Composites of Carbon and Spinel Oxides

As substitutes for expensive noble metal catalysts, spinel oxides [denoted as $A_xB_{3-x}O_4$ (A, B=Co, Zn, Ni, Fe, Cu, Mn, etc.)] have gained much attention because of their low costs, considerable activities, high abundance (stability), and environmental friendliness [136–138]. To achieve better catalytic activities toward ORR and OER, however, net spinel oxides are usually attached onto conducting carbon substrates with the aim of assuring fast electron transport and good interaction between oxides and carbon [136]. For example, Li et al. [137] performed an in situ growth of spinel $CoFe_2O_4$ nanoparticles on rod-like ordered mesoporous carbon (CFO/RC) through a hydrothermal treatment process with an annealing procedure in which $Co(NO_3)_2{\cdot}6H_2O$ and $Fe(NO_3){\cdot}9H_2O$ were used as Co and Fe sources. According to different annealing temperatures of 300, 400, 500, and 600 °C, the final composites were labeled as CFO/RC-300, CFO/RC-400, CFO/RC-500, and CFO/RC-600, respectively. In the examination of surface chemical composition and

cation oxidation states using XPS, no shifts were found for the Co 2*p* peaks of the pure CFO and CFO/RC-400 catalysts, indicating that the Co cations in both catalysts possessed the same chemical surrounding. For the Fe $2p_{3/2}$ and Fe $2p_{1/2}$ of the Fe 2*p* spectra, however, CFO/RC-400 showed two small shifts to higher binding energies as compared with CFO, revealing strong coupling between CFO and RC. In further analyses, the O1*s* peak of CFO/RC-400 was seen to shift to higher binding energies in comparison with CFO, confirming the strong coupling between CFO and RC from the lattice oxygen in the Co/Fe–O framework during the hydrothermal treatment. In the assessment of electrocatalytic properties, LSV curves (Fig. 8a) in O_2-saturated 0.1 M KOH solution at a rotation rate of 1600 r min^{-1} showed that all CFO/RC composites exhibited superior onset potentials (− 0.10 to − 0.13 V) compared with CFO (− 0.23 V) and RC (− 0.29 V). This was attributed to the synergistic effects of the two components as well as the large amount of defected CFO nanoparticles providing more active sites. For Tafel plots in the low overpotential region, the Tafel slope (99 mV per dec) of the CFO/RC-400 composite was lower than those of CFO (129 mV per dec) and RC (125 mV per dec). Both results indicate that CFO/RC-400 possessed enhanced ORR kinetics after the incorporation of CFO into RC. Among all CFO/RC composites, CFO/RC-400 produced the highest limiting current density (4.86 mA cm^{-2}) and the highest onset potential (~ − 0.10 V), indicating that CFO/RC-400 possessed the optimal ORR activity among all CFO/RC composites. This is not only because annealing temperatures below 400 °C can result in the incomplete CTAB decomposition covering some active sites, but also because annealing temperatures above 400 °C can cause the reduction of defects and the increase of particle sizes, decreasing electrocatalytic activity. For OER, anodic LSV curves (Fig. 8b) were recorded in N_2-saturated 0.1 M KOH solution at a rotation speed of 1600 r min^{-1}. Here, both the onset potential and Tafel slope (in the low overpotential region) of CFO/RC-400 (~ 0.41 V, 92 mV per decade) were less than those of CFO (~ 0.43 V, 112 mV per decade), RC (~ 0.75 V, 308 mV per decade), and 20 wt% Pt/C (~ 0.54 V, 105 mV per decade). At 1.0 V, CFO/RC-400 displayed a much higher current density of 39.6 mA cm^{-2} than CFO (~ 34.5 mA cm^{-2}), RC (~ 3.37 mA cm^{-2}), and Pt/C (~ 27.8 mA cm^{-2}), demonstrating the much higher OER activity of CFO/RC-400 as compared with CFO, RC, and Pt/C samples. This can possibly be attributed mainly to the hierarchical mesoporous structure of the RC matrix and the strong coupling and synergistic effects between CFO and RC. Based on the obtained ORR and OER activities, the CFO/RC-400 composite was also found to outperform other carbon-spinel oxide composite catalysts such as $NiCo_2O_4$/grapheme [139], $CoFe_2O_4$/grapheme [140], and $CoFe_2O_4$/biocarbon [141], suggesting that ordered mesoporous carbon rods are more suitable for spinel oxide nanoparticle loading to improve ORR and OER than other carbon matrixes such as CNTs, graphene, and biocarbon materials.

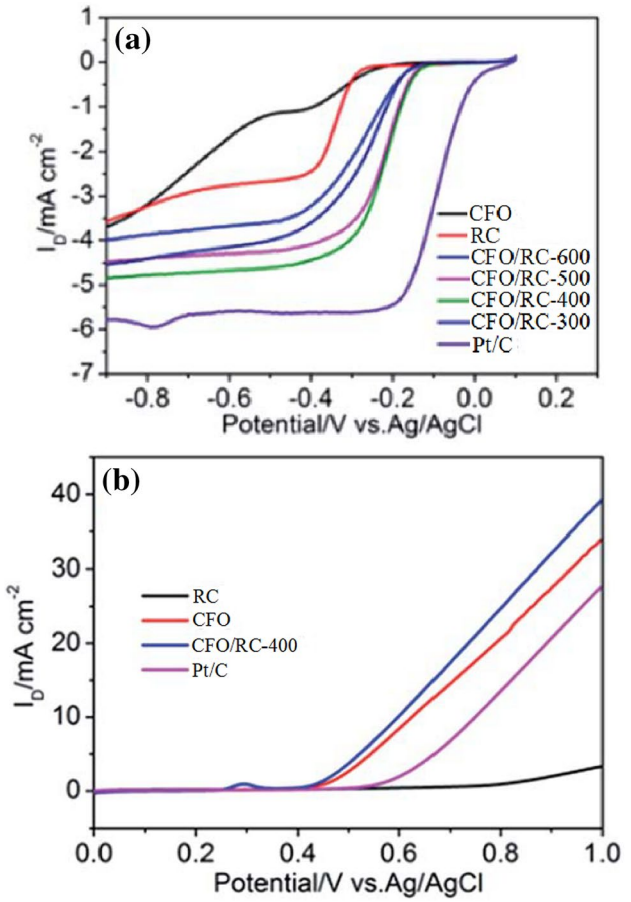

Fig. 8 **a** Linear sweep voltammetry (LSV) of RC, CFO, CFO/RC composite and commercial Pt/C in O_2-saturated 0.1 M KOH solution at a rotation rate of 1600 r min^{-1}, and **b** anodic LSV of RC, CFO, CFO/RC-400 composite and commercial Pt/C in N_2-saturated 0.1 M KOH solution at a rotation rate of 1600 r min^{-1}. Reprinted with permission from Ref. 137 Copyright 2016 Royal Society of Chemistry

Similar to $CoFe_2O_4$ and $NiCo_2O_4$ ternary spinel oxides, Co_3O_4; a binary spinel oxide, has also been investigated in the development of carbon-spinel oxide bifunctional composite catalysts. Specifically, a facile hydrothermal route was used by Liu et al. [142] to form a cubic Co_3O_4 and multi-walled carbon nanotube (cCo_3O_4/MWCNT) composite in which MWCNTs were acid-functionalized as structure directing/oxidizing agents and $Co(CH_3COO)_2{\cdot}4H_2O$ was used as the single Co source. For comparison, pure cCo_3O_4, acid-treated MWCNTs and a physical mixture of cCo_3O_4 + MWCNTs were chosen as reference samples. The comparison of XRD patterns of cCo_3O_4 and cCo_3O_4/MWCNTs revealed that after their spinel structures were confirmed, the peaks of cCo_3O_4 were shifted slightly to a larger 2θ angle after the addition of MWCNTs, suggesting a

slight lattice contraction possibly due to variations in crystal sizes [143, 144] or interactions between cCo_3O_4 and MWCNTs. SEM and TEM images confirmed the cubic morphology of cCo_3O_4 and showed the attachment of MWCNTs to the cCo_3O_4 surface without free cubic particles. These results indicated the effective tethering between MWCNTs and cCo_3O_4 as the acid-functionalized MWCNTs served as an oxidizing/structure directing agent to oxidize cobalt ions into spinel cobalt oxides and regulate the formation of cubic cobalt oxide. According to TGA, the cCo_3O_4/MWCNTs composite contained 54% cCo_3O_4, similar to the physical mixture of cCo_3O_4 + MWCNTs. For ORR, LSV curves in O_2-saturated 0.1 M KOH solution showed that among all tested catalysts, cCo_3O_4/MWCNTs possessed the largest onset potential (~ − 0.15 V) and best current density (~ − 2.91 mA cm^{-2} at − 0.4 V), indicating that cCo_3O_4/MWCNTs possessed superior ORR activity to cCo_3O_4, MWCNTs, and cCo_3O_4 + MWCNTs. For OER, LSV curves in N_2-saturated 0.1 KOH solution showed that cCo_3O_4/MWCNTs possessed the best OER activity as evidenced by a higher current density (~ 16.0 mA cm^{-2} at 0.7 V) compared with other catalysts. A further cycling test with 500 continuous CV cycles showed that the ORR current density of cCo_3O_4/MWCNTs was about 4, 34, and 3 times better than the MWCNTs, cCo_3O_4, and cCo_3O_4-MWCNTs catalysts, respectively, and that the final OER current density of cCo_3O_4/MWCNTs was 49% higher than cCo_3O_4-MWCNTs and greater than the individual components. These results suggested that cCo_3O_4/MWCNTs can produce stronger interactions between cCo_3O_4 and MWCNTs, resulting in possible coupling effects and thus higher ORR and OER activities.

5.3 Composites of Carbon and Other Oxides

Apart from perovskite oxides and spinel oxides, other oxides, such as CoO [145, 146], MnO_2 [147, 148], and RuO_2 [149, 150], have also been used to prepare effective carbon-composited bifunctional catalysts to tackle the sluggish kinetics of ORR and OER in MABs. Based on a novel strategy to improve the catalytic performance of CoO through the integration of dotted carbon species and oxygen vacancies, Gao et al. [145] designed and synthesized a carbon-dotted CoO with oxygen vacancies (CoO/C) for LAB cathodes using a simple calcination of a formed pink precipitate of ethanol-mediated $Co(Ac)_2{\cdot}4H_2O$. In their structure characterizations, XRD spectra were used for the low composition of $CoO_{0.89}$ from Rietveld refinement. Furthermore, the Raman spectra was used for analysis of the shift of Co–O vibration peaks for both CoO and CoO/C, and revealed a negative shift of Co–O signal for CoO/C as compared to CoO due to suggested oxygen vacancies. This was further confirmed by thorough XPS analysis of both Co 2*p* and O 1s signals. A Co 2*p* spectra was only fitted with one peak related to Co^{2+} in CoO/C, while two spin orbit doubles of Co^{2+} and Co^{3+} has been assigned in their CoO reference sample. In addition, analysis of O 1S showed the shift of O4 signal, resulting from CoO reduction (O-to-Co atomic ratio was less than calculated 1.39) in CoO/C sample. This indicated on existence of oxygen deficiencies in the CoO/C sample after the addition of C species. In their evaluation of battery performance and electrocatalyst activities for both ORR and OER, the CoO/C catalyst showed larger capacities (~ 7011 and ~ 4074 mAh g^{-1} at 100 and 400 mA g^{-1}, respectively) than CoO (~ 5189, ~ 2059 mAh g^{-1}), and cyclability tests in a rechargeable LAB with a current density of ~ 200 mA g^{-1} and a high voltage cutoff of 4.5 V demonstrated that CoO/C can achieve higher cycle numbers (50) than CoO. These results indicate that the addition of carbon can significantly improve electrocatalytic activities for both ORR and OER. A further investigation of morphology and phase composition under different charge/discharge states using SEM and XRD demonstrated that the main discharge product, Li_2O_2, can be completely decomposed by CoO/C but not by CoO. This quality attributed to the lower charge–discharge overpotentials and higher cycling properties of CoO/C. Overall, these enhanced electrochemical performances can be attributed to the composition between carbon and CoO and can possibly be associated with the integration of carbon dotting and oxygen vacancies into CoO as well as the synergetic effects of the two components. This promising strategy of compositing carbon with oxides to create positive effects on MAB ORR and OER has inspired more research into exploring and using different oxides, such as La_2O_3 [151], zirconium doped ceria [152], and cobalt-manganese mixed oxide ($Co_xMn_{1-x}O$) [153].

6 Composites of Carbon and Nitrides

Combining carbon and nitrides (e.g., TiN or CN) to create novel catalysts for MAB ORR and OER has become an effective strategy to improve rechargeability and round-trip efficiency. Titanium nitride (TiN), a typical transition metal nitride with high electronic conductivity and good electrochemical activity, is widely applied in electrochemistry studies [154]. Using a template method (Fig. 9a), Li et al. [155] prepared nano-sized TiN supported on Vulcan XC-72 (*n*-TiN/VC) and used this as a bifunctional catalyst for non-aqueous LABs. Commercial micrometer scale TiN was used by the researchers to prepare *m*-TiN/VC samples as reference. XRD patterns revealed that TiN in *n*-TiN/VC possessed a crystallite size of 4.3 nm according to the Scherrer equation and was consistent with TEM results. BET measurements showed that the surface areas of the *n*-TiN/VC, *m*-TiN/VC, and VC samples were 172, 144, and 233 m^2 g^{-1} respectively. In electrochemical measurements,

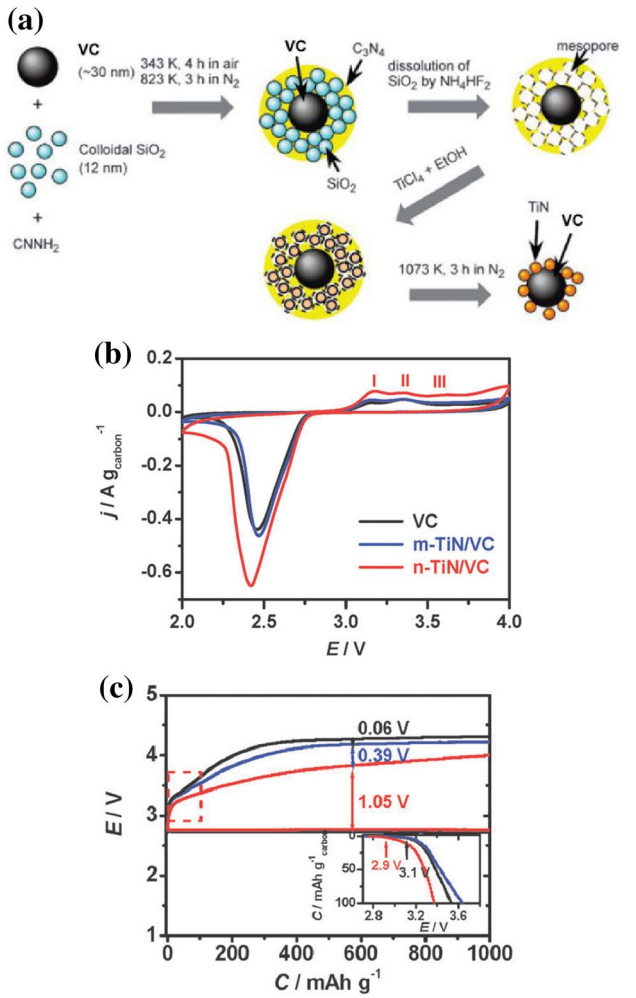

Fig. 9 **a** Preparation process of *n*-TiN/VC. **b** CV curves of LAB with VC, m-TiN/VC, and *n*-TiN/VC as air-electrode catalysts under an O_2 atmosphere from 2.0 to 4.0 V at 0.05 mV s^{-1}. **c** Discharge-recharge curves of VC, *m*-TiN/VC, and *n*-TiN/VC as cathode catalysts for LABs with an enlarged section highlighted (inset) at 50 mA g^{-1}_{carbon}. Reprinted with permission from Ref. [155]. Copyright 2013 Royal Society of Chemistry

CVs (Fig. 9b) under O_2 from 2.0 to 4.0 V at a scan rate of 0.05 mV s^{-1} in a LAB revealed that for the cathodic scan, *n*-TiN/VC showed higher ORR currents than *m*-TiN/VC and VC cathodes. For the anodic scan, *n*-TiN/VC presented three oxidation peaks rather than two as seen in the CVs of *m*-TiN/VC and VC cathodes. This suggests three varied OER pathways [i.e., I: Eq. (1), II: Eq. (2), and III: Eq. (3)] according to the decomposition mechanisms [156, 157]:

$$LiO_2 \rightarrow Li^+ + O_2 + e^- \quad (1)$$

$$Li_2O_2 \rightarrow 2Li^+ + O_2 + 2e^- \quad (2)$$

$$2LiO_2 \rightarrow 4Li^+ + O_2 + 4e^- \quad (3)$$

For OER curves (Fig. 9c) at 50 mA g^{-1}_{carbon}, *n*-TiN/VC provided the lowest recharge voltage and accordingly the lowest voltage gap (~ 1.05 V), showing promoted OER activity. Moreover, the initial section of the recharge in the inset of Fig. 9c shows a lower onset potential (~ 2.9 V) for *n*-TiN/VC than those of *m*-TiN/VC (~ 3.1 V) and VC (~ 3.1 V) cathodes, matching the strong oxidation peak of LiO_2 produced by *n*-TiN/VC as shown in Fig. 9b, demonstrating better OER activities due to the interaction between *n*-TiN and VC. In five discharge–recharge cycles, *n*-TiN/VC exhibited higher recharge voltages at the 5th discharge–charge cycle than both *m*-TiN/VC and VC cathodes. This can be attributed to the strong interaction between the remaining Li_2O_2 deposits and the TiN nanoparticles on the carbon surface, resulting in high stability. However, because TiN can be oxidized to TiO_2 based on the results of XRD and FTIR, LABs with *n*-TiN/VC cathodes possess a limited potential of 4.3 V despite its ability to enhance ORR and OER. Park et al. [158] studied TiN/C composites and found that the porous structure and synergistic effects between TiN and carbon play a promoting role in the enhancement of catalytic activity for both ORR and OER in LABs.

Graphitic carbon nitride (g-CN) is also an attractive metal-free material because of its abundance and negligible metal pollution [159]. However, the ORR activity of g-CN itself is not satisfactory because of its poor electrical conductivity [160, 161] despite nitrogen atoms in g-CN being able to increase the electropositivity of adjacent carbon atoms. Based on this, Fu et al. [162] combined carbon with porous graphitic g-CN through a template-free synthesis route to obtain g-CN/C composite catalysts for ORR in MABs. In their experiment, based on the amount of D-glucose (i.e., 15.84, 39.60, and 79.20 mmol) used, three g-CN/C samples (g-CN/C-1, g-CN/C-2, and g-CN/C-3) were obtained. For comparison, a physically mixed g-CN and carbon, labeled as g-CN + C, was also prepared. The addition of carbon increased not only the BET surface area but also porosity. Table 4 presents the ratio of CN in the g-CN in terms of the atomic ratio of carbon and nitrogen as well as the relative composition ratios (%) of the four samples derived from XPS spectra. A comparison of ORR activities for the three different composites (i.e., g-CN/C-1, g-CN/C-2, and g-CN/C-3) revealed that g-CN/C-2 with 33.75 wt% N content delivered a more positive potential and a larger limiting current than g-CN/C-1 (~ 50.35 wt% N) and g-CN/C-1 (~ 26.09 wt% N) samples, demonstrating that g-CN/C-2 possessed the best ORR activity. This result suggests that high N content benefits the tradeoff between available ORR active sites and electron conduction. LSV curves of g-CN/C-2 obtained in O_2-saturated 0.1 M KOH solution at 1600 r min^{-1} exhibited significantly more positive onset potentials (~ 0.90 V) and larger disk currents (limiting current density, 4.10 mA cm^{-2}) than those of the

Table 4 Ratios of CN in g-CN based on the atomic ratio of carbon and nitrogen and relative composition ratio (%) of four carbon components derived from the deconvoluted XPS spectra. Reprinted with permission from Ref. [162]. Copyright 2016 Royal Society of Chemistry

Samples	C1*s* (atm.%)[a]	N1*s* (atm.%)	Relative composition ratio of carbon (%)[b]				C/N[c] in g-CN
			P1	P2	P3	P4	
g-CN	50.74	43.11	42.72	0	0	57.28	0.67
g-CN/C-1	74.60	15.61	37.84	20.75	30.22	11.18	0.53
g-CN/C-2	74.70	19.88	29.03	27.51	25.03	18.43	0.69
g-CN/C-3	76.40	16.57	39.34	12.09	29.05	19.52	0.90

[a]Atomic ratios of carbon and nitrogen in composites are obtained from XPS results

[b]Different carbon percentages deconvoluted from the C1*s* XPS spectra of composites

[c]The ratio of C/N in g-CN is calculated based on the carbon present in C–N bonds divided by nitrogen according to the equation C/N = P4 * C1*s*/N1*s*

g-CN and g-CN + C samples, confirming the higher ORR activity of g-CN/C-2. Current-time chronoamperometric responses in O_2-saturated 0.1 M KOH solution showed that after 20,000 s, g-CN/C-2 decayed less (~ 20%), displaying superior stability compared with g-CN + C. All these results demonstrate the high ORR activity and good stability of the g-CN/C-2 catalyst. Recently, doping strategies (e.g., P-doping) have also been used to fabricate P-doped g-CN for MAB applications [163] in which in situ growth of P-g-C_3N_4 on carbon-fiber paper (PCN-CFP) is carried out for ZAB flexible oxygen electrodes. These resultant PCN-CFP catalysts exhibit outstanding ORR and OER activity, stability, and reversibility in tested ZABs.

7 Composites of Carbon and Carbides

Because carbides possess desirable ORR activities [164], researchers have recently attempted to utilize carbides such as tungsten carbide (WC) [165] and boron carbide (B_4C) [166] to create carbon-composited catalysts to improve capacity, rechargeability, and round-trip efficiency in MABs. For example, Koo et al. [165] coated a uniform WC layer onto a carbon (Ketjenblack EC600-JD) cathode using physical vapor deposition (PVD) (Fig. 10a) with TEM images revealing a 20-nm-thick uniform WC-coating layer and electrochemical measurements being performed in a non-aqueous LAB (Fig. 10b). The obtained discharge curves (down to 2.0 V) show that the WC-coated cathode can deliver a capacity of ~ 7000 mAh g^{-1}_{carbon}. This is twofold higher than that of the carbon cathode. Additionally, it was found that in the comparison of the 1st discharge–charge curve and the 10th discharge–charge curve at 100 mA g^{-1}_{carbon}, the WC-coated cathode produced lower overpotential gaps of 700 and 1200 mV as compared with those of the carbon cathode. These results suggest that WC coating can enhance both ORR and OER and therefore limit discharge–charge overpotentials due to the

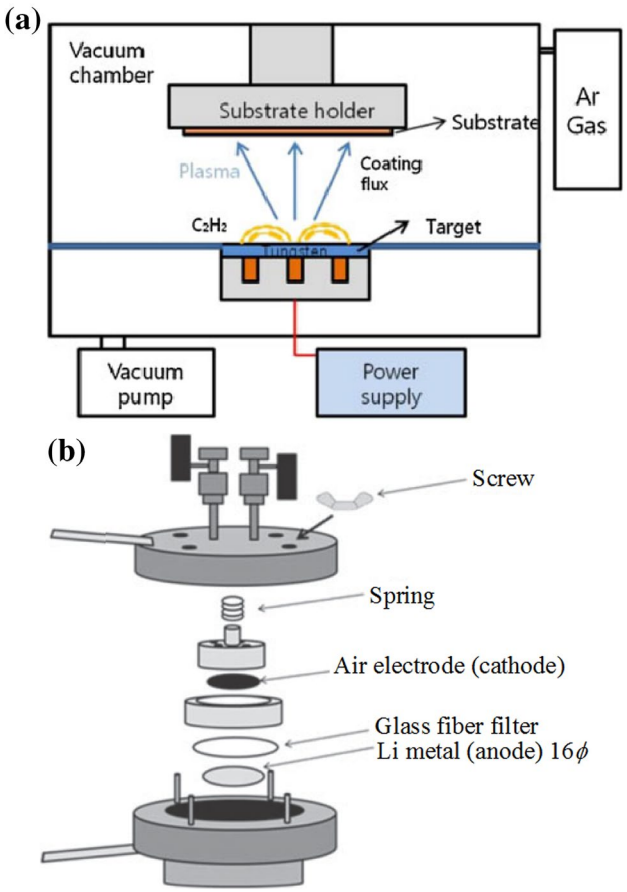

Fig. 10 **a** Schematic diagram of PVD method for WC coating. **b** Design and configuration of LAB. Reprinted with permission from Ref. [165]. Copyright 2015 IOP publishing

enhanced catalytic property and electrical conductivity of the carbon-WC composite. In further tests, at a current density of ~ 1000 mA g^{-1}_{carbon} and a voltage range of 2.0–4.2 V, the WC-coated cathode was found to be able to be efficiently operated beyond the 36th cycle, whereas the carbon cathode stopped operating at the 12th cycle. This

increased cycle stability and round-trip efficiency clearly demonstrates the improvements in reaction rates and the reduction in discharge and charge voltage gaps. Moreover, it was shown that during the charge and discharge cycling process, the addition of WC resulted in the rapid creation and decomposition of reaction products (i.e., Li_2O_2) because of the enhanced catalytic effects. And as current densities increased from 100 to 200 mA g^{-1}_{carbon}, the WC-coated cathode also showed decreased overpotentials compared with the carbon cathode, further confirming the benefits of WC coating.

Similar to the WC-C composite above, B_4C nanowires-carbon nanotube (BC) composite cathodes, induced by the synergistic effect of B_4C and carbon, were also found to exhibit improved ORR/OER activity, rechargeability, and round-trip efficiency for LABs by Luo et al. [166]. In their typical experiment, Raman spectra, field emission scanning electron microscopy (FESEM), STEM, and EDS were used for characterizations to confirm the formation of carbon-B4C composites. Their Raman spectra showed bands below 1200 cm^{-1}, which matched the characteristics of B_4C [167, 168], and FESEM, STEM and EDS confirmed a large amount of B_4C nanowires growing from CNT aggregations that possessed diameters in the range of 40–100 nm, and lengths above 2 μm. In RDE measurements in O_2-saturated 0.1 M KOH at a scan rate of 10 mV s^{-1}, LSV curves at 900 r min^{-1} showed that the B–C composite exhibited a more positive onset potential and a larger current density, corresponding to a higher ORR activity in comparison with those of the Pt/C and CN samples. Based on Koutecky–Levich plots, the B–C composite was revealed to produce a nearly four-electron ORR process comparable to Pt/C (n ~ 4.0) but different from CN (n = 3.2–3.5). Subsequent comparisons of OER curves revealed that the B–C composite provided a smaller Tafel slope of ~ 70 mV per decade than Pt/C (~ 123 mV per decade), indicating that the B–C catalyst possessed superior OER activity to 20 wt% Pt/C. Electrochemical properties were continuously tested in an assembled battery with B–C and CN composite cathodes and the researchers found that the B–C composite showed not only higher ORR potential and lower OER potential compared with CN, it also exhibited better cycling performances with a higher round-trip efficiency. These results can possibly be attributed to B_4C and carbon providing efficient synergistic effects on electrocatalytic reactions.

8 Other Carbon-Based Composites

Other carbon-based composites can be classified into carbon-based binary composites and ternary composites in which strong synergistic effects between different components are found to enhance electrocatalytic ORR and OER performances in MABs.

8.1 Other Carbon-Based Binary Composites

To develop high-performance bifunctional catalysts and solve carbon corrosion issues in MABs, Lyu et al. composited cobalt sulfide, acting as an active ORR material, with carbon to form carbon-based binary composites for cathode materials in MABs [169]. In their experiment, cobalt acetate ($Co(Ac)_2$) and thioacetamide were used as Co and sulfur sources to obtain a novel CoS_2 nanoparticles-reduced graphene oxide (CoS_2/*r*GO) composite for aprotic LABs. TGA revealed 78 wt% CoS_2 and XRD showed that the patterns of cobalt sulfide on the graphene sheet were of a typical cubic CoS_2 phase (JCPDS 00-41-1471). In measurements in an aprotic LAB using $LiClO_4$-DMSO as an electrolyte, the CV curves showed that the CoS_2/*r*GO cathode delivered a higher ORR onset potential and a notably higher OER current peak (at ~ 3.75 V), demonstrating its higher catalytic activities for both ORR and OER than those of *r*GO and Vulcan XC-72. A combination of XRD, XPS, and SEM revealed the significant role of CoS_2 in lowering discharge/charge overpotentials by positively affecting the formation and decomposition of Li_2O_2. Here, Li_2CO_3 is still formed as a side product during discharging/charging, however. In measurements of rate capability and cyclability, it was found that although rate capabilities increased with increasing rates from 50 to 500 mA g^{-1}, CoS_2/*r*GO only ran 18 cycles in the cycling test at a rate of 200 mA g^{-1} and a limited capacity of 500 mAh g^{-1}. This indicates possible incomplete decomposition of side products (e.g., Li_2CO_3). Therefore, carbon–cobalt sulfide composites need to be further improved in future studies to improve its potential in the development of advanced bifunctional catalysts for LABs.

$NiCo_2S_4$ was also combined with *r*GO to synthesize $NiCo_2S_4$–*r*GO composites by Wu et al. [170] and their research found that the synergistic effects between $NiCo_2S_4$ and *r*GO can result in superior ORR performances as compared with 20 wt% Pt/C, demonstrating potential as a bifunctional catalyst in MABs. Aside from sulfides, other functional materials, such as FeOOH [171], soil [172], polyimides [173], and Fe phthalocyanine (FePc) [174], have also used in the development of carbon-based binary composites for MAB bifunctional catalysts. In these studies, the incorporation of these functional materials yielded active synergistic effects with carbon, producing active sites for enhanced ORR and OER and reducing side reactions in electrocatalytic reactions to improve cycling performances and catalytic stability.

8.2 Other Carbon-Based Ternary Composites

Based on the synergistic effects of three separate components and their inter-correlation, various researchers have recently focused on developing carbon-based ternary composites as advanced cathodes in MABs. Among carbon-based ternary composites for MABs, carbon; coupled with an oxide, is usually combined with a third component such as a polyelectrolyte [175], a second oxide [176], or a metal [177] to exhibit enhanced catalytic activities toward ORR and/or OER and improved MAB performance. A positively charged polyelectrolyte, poly(diallyldimethylammonium chloride) (PDDA), was used by Zhai et al. [175] to modify carbon supports to provide available functional groups favorable to the formation of more active sites. In their study, PDDA functionalized CNTs were combined with spinel $CoMn_2O_4$ to form a ternary $CoMn_2O_4$/PDDA-CNTs composite ORR catalyst. Their results showed that by increasing the loading of $CoMn_2O_4$ from 36 to 83 wt%, the $CoMn_2O_4$/PDDA-CNTs composite exhibited high ORR current densities in alkaline and neutral conditions through a 4e reduction pathway that outperformed Pt/C due to the non-covalent coupling effects between $CoMn_2O_4$ and PDDA-CNTs. Moreover, at an optimal content of 36 wt% $CoMn_2O_4$, the $CoMn_2O_4$/PDDA-CNTs potential difference between ORR and OER was ~ 0.849 V, demonstrating potential bifunctionality. To obtain a suitable third component, Ma and Wang [176] selected two different oxides to fabricate α-MnO_2–$LaNiO_3$/CNTs composites with the expectation that α-MnO_2 and $LaNiO_3$ can produce synergistic effects on bifunctional activity. According to the literature [4, 5, 126, 130], α-MnO_2 acts as a good ORR catalyst and $LaNiO_3$ as a good OER catalyst. Their experiment showed that the α-MnO_2–$LaNiO_3$/CNTs cathode provided excellent charge–discharge cycling performances within 75 charge–discharge cycles due to good bifunctional activity and durability. Wu et al. [177] studied Ni-modified MnO_x/C (Ni-MnO_x/C) composites for ORR and their application in ZABs and they demonstrated that at an optimal Ni/Mn atomic ratio of 1:2, Ni-MnO_x/C cathodes in a tested ZAB can achieve a large power density of ~ 122 mW cm^{-2}. This was better than MnO_x/C (~ 89 mW cm^{-2}) and slightly higher than referenced cathodes of Pd/C (~ 121 mW cm^{-2}) and Pt/C (~ 120.5 mW cm^{-2}).

Other carbon-based ternary composites such as Fe/Fe_3C–CNFs [113] and Fe-doped NiOOH grown on graphene-encapsulated $FeNi_3$ nanodots ($FeNi_3$@GR@Fe–NiOOH) [114] were also studied by Wang et al. for MAB ORR and OER. In these two carbon-based ternary composites, carbon provided an excellent porous structure and high surface area, whereas the other two components provided electrochemical properties associated with their catalytic performance (i.e., ORR and OER) and physiochemical properties (e.g., active sites, thermal ability, conductivity, and chemical/physical stability). For all components, the synergistic effects can be observed improving the catalytic activities and cycling performances of MABs. Table 5 shows the electrochemical performances of typical metal-free carbon-composited bifunctional catalysts for MAB cathodes [145, 146, 148–150, 152, 158, 165, 166, 171–174, 176, 178–183].

Metal-free catalysts composed of carbon and other components (e.g., oxides, nitrides, carbides, sulfides, β-FeOOH, polyimide, Fe phthalocyanine, etc.) have been intensely studied as cathode materials for MABs and the results show advantages over pure carbon in terms of ORR/OER activity and cycling stability/durability. For example, polyimide/CNT catalysts [173] have been found to exhibit a high cycling stability over 130 cycles with a maximum discharge capacity of 11,000 mAh g^{-1} at a high current density of 500 mA g^{-1} under LAB operation conditions. As discussed previously, the combination of carbon and oxide(s) is a sound strategy in the development of abundant, low-cost, and efficient bifunctional catalysts for rechargeable MABs owing to the strong synergy between carbon and oxides. For example, MnO_x/CP [148] and $CoMn_2O_4$/*r*GO [179] can achieve 500 and 200 cycles at 15 and 20 mA cm^{-2}, respectively, indicating a significant improvement of cycling performances due to strong resistances to carbon corrosion. A SP/$CaMnO_3$ catalyst [181] demonstrated charge–discharge stability after over 80 cycles (with a high current density of 200 mA g^{-1} and a limited capacity of 1000 mAh g^{-1}) and high discharge capacities of 7000 mAh g^{-1}. These results demonstrate the beneficial effects of combining different components with carbon material in terms of electrocatalytic activity, stability/durability, and associated MAB performances. However, further improvements and studies are needed to enhance MAB performances to achieve commercialization.

Nevertheless, based on the collected data for several types of bifunctional catalysts in Tables 2, 3 and 5, the cycling performances of ORR and OER are not easily improved even with the use of different components compositing with carbon. This may be because the nanostructure and property of the formed carbon composites are closely associated with discharge products during cycling. In a comparison of stability, Co/C/NiFe LDH/AB and Co–N/C composite catalysts in Table 3 show 300 cycle numbers at 40 mA cm^{-2} and 500 cycle numbers at 2 mA cm^{-2} respectively, whereas the MnO_x/CP catalyst in Table 5 produces 500 cycle numbers at 15 mA cm^{-2}. These results indicate a successful strategy without the use of noble metals in developing high-performance catalysts with high bifunctional activities and stability. For the scale-up production of next-generation bifunctional catalysts in commercial MABs, low costs, high bifunctional activities, and good stability are strongly desired. In terms of material cost and availability, noble metals are being replaced by low-cost materials such as transitional metals, oxide, nitrides, carbides, sulfides, β-FeOOH, Fe phthalocyanine, and conducting polymers to

Table 5 Electrochemical performance for typical metal-free carbon-composited bifunctional catalysts as air-electrode materials in the tested MABs

No.	Bifunctional catalyst as cathode materials	Maximum capacity/mAh g^{-1} (current density/[a]mA g^{-1} or [b]mA cm^{-2})	Cycle number (current density/mA g^{-1} or mA cm^{-2}, upper-limit capacity/mAh g^{-1})	Potential range for cycle testing (V)	Potential difference for ORR/OER (initial ORR/OER overpotentials[c], V vs. Li/Li^+)	Energy efficiency (%)	Electrolyte type	MAB type	References
1	CoO/SP	5637 (200[a])	50 (200[a], 1000)	2.0–4.5	1.32 (2.63/3.95)	–	1 M LITFSI/TEGDME	rLOB	[145]
2	CoO/CNF	3882.5 (0.2[b])	50 (0.2[b], 1000)	2.0–4.2	1.08 (2.72/3.80)	–	1 M LiTFSI/TEGDME	rLOB	[146]
3	MnO_x/CP	–	500 (15[b], –)	1.0–2.4	0.75 (1.25/2.00)	–	6 M KOH +20 g L^{-1} $ZnCl_2$	rZAB	[148]
4	RuO_2/CNT	1150 (0.4[b])	50 (0.4[b], 244)	2.0–4.4	1.38 (2.56/3.94)	65.4%	1 M LITFSI/TEGDME	LOB	[149]
5	RuO_2·0.64H_2O/*r*GO	5000 (500[a])	35 (200[a], 2000)	2.0–4.3	1.40 (2.75/4.15)	–	$LiCF_3SO_3$/TEGDME (1:4 mol/mol)	LOB	[150]
6	G/Zr–CeO_2	3254 (0.2[b])	15 (1[b], 500)	2.0–4.5	1.60 (2.50/4.10)	–	1 M LITFSI/TEGDME	LOB	[152]
7	TiN/C	7100 (100a)	35 (200[a], 1000)	2.0–4.5	1.15 (2.60/3.75)	–	$LiCF_3SO_3$/TEGDME (1:4, mol/mol)	LOB	[158]
8	WC/C	7000 (100[a])	36 (100[a], 1000)	2.0–4.5	0.88 (2.75/3.63)	–	1 M LITFSI/TEGDME	LOB	[165]
9	B_4C/CNT	16,000 (0.2[b])	120 (0.4[b], 1000)	2.5–4.4	1.02 (2.73/3.75)	–	$LiCF_3SO_3$/TEGDME (1:4, mol/mol)	LOB	[166]
10	β-FeOOH/C aerogels, β-FeOOH/Super P	10,230 (0.1[b]), 6050 (0.1[b])	60 (0.1[b], 800), 42 (0.1[b], 800)	2.0–4.4	1.22 (2.69/3.91)	–	1 M LITFSI/TEGDME	rLOB	[171]
11	VC/soil	7640 (0.2[b])	100 (0.2[b], 1000)	2.3–4.2	1.59 (2.71/4.30)	–	1 M LITFSI/TEGDME	rLOB	[172]
12	Polyimide/CNT	11,000 (500[a])	137 (500[a], 1500)	2.0–4.35	1.72 (2.63/4.35)	–	1 M LITFSI/TEGDME	LAB	[173]
13	FePc/GNS, FePc/CNTs, FePc/AB	865.6 (0.5[b]), 632.4 (0.5[b]), 795.4 (0.5[b])	30 (0.5[b], –), 30 (0.5[b], –), 30 (0.5[b], –)	2.0–4.8	0.67 (3.00/3.67), 0.85 (3.02/3.87), 1.05 (2.82/3.87)	–	1 M $LiClO_4$/ED/DEC + 1 M $LiNO_3$/0.5 M LiOH	LAB	[174]
14	MnO_2–$LaNiO_3$/CNT	–	75 (20[b], –)	0.8–2.4	0.75 (1.20/1.95)	–	6 M KOH + 0.4 M ZnO	rZAB	[176]
15	CNT/$CoFe_2O_4$	3670 (200a)	35 (200[a], 430)	2.0–4.3	1.55 (2.70/4.25)	–	1 M LITFSI/TEGDME	rLOB	[178]
16	$CoMn_2O_4$/*r*GO	610 (20[b])	200 (20[b], –),	0.8–2.4	0.95 (1.15/2.10)		6 M KOH	ZAB	[179]
17	VC/Co_3O_4	–	22, (20[b], –),	0.5–3.0	1.25 (1.00/2.25)	–	6 M KOH + 0.2 M Zinc acetate	rZAB	[180]
18	SP/$CaMnO_3$	7000 (200[a])	80 (200[a], 1000)	2.0 -4.0	1.50 (2.25/3.75)	–	1 M $NaSO_3CF_3$/TEGDME	NaOB	[181]
19	KB/RM-TIT[m], KB/RM-FIT[n], KB	3250 (100[a]), 2700 (100[a]), 5950 (100[a])	121 (400[a], 1000), 105 (400[a], 1000), 24 (400[a], 1000)	2.0–4.8	0.74 (2.76/3.50), 1.25 (2.75/4.00), 1.70 (2.68/4.38)	–	1 M LITFSI/TEGDME	rLOB	[182]
20	CNT@RuO_2	4350 (100[a])	100 (500[a], 300)	2.3–4.0	0.72 (2.70/3.42)	–	LITFSI/tri(ethylene) glycol dimethyl ether (1:5 mol/mol)	rLOB	[183]

[a]mA g^{-1}

[b]mA cm^{-2}

[c]Initial overpotentials are obtained from the cyclic tests

[m]RuO_2 tube in Mn_2O_3 tube

[n]RuO_2 fiber in Mn_2O_3 tube

composite with carbon to enhance bifunctional activities and stability. With the rapid development of nanotechnologies and related sciences, processing techniques are becoming more facile in the fabrication of non-noble metal-based and metal-free bifunctional catalysts in scale-up productions.

9 Summary, Challenges and Future Research Directions

9.1 Summary

In this review, carbon-composited bifunctional catalysts for MABs are comprehensively reviewed in terms of their material selection, synthesis method, structural characterization and electrochemical performance. Compared with single material catalysts, composited catalysts possess synergistic effects on structural and electrical properties resulting from different components, leading to enhanced ORR and OER performances in MAB air-electrode catalysts. In the design of advanced carbon-based composites as bifunctional catalysts, the proper selection of carbon materials is crucial because the properties of the carbon material (e.g., porous structure, surface area and electronic conductivity) affect the transport of ionic/electronic/gas, electron conductivity and the distribution of catalytic sites. In addition, the strong interaction between the carbon materials with other component(s) determines the bifunctional activities of ORR and OER and their stability/durability. As compared with other porous structures, (i.e., macropore and microporous structures), it is known that mesoporous structures coupled with high surface areas are more beneficial to ionic and electronic transport because of shorter conducting paths. Mesoporous structures also possess the ability to retain electrocatalytic active sites with uniform distribution.

As a special type of carbon material, graphene tends to hold active sites at the edge rather than the mesoporous structure. However, the restacking of graphene layers is a vital issue that needs to be resolved in the development of advanced graphene-composited bifunctional catalysts for MABs.

It is should also be emphasized that not all non-carbon material(s) are able to act as useful component(s) in carbon-composited bifunctional catalysts in terms of producing synergistic interactions and overcoming carbon corrosion/oxides in MABs. Heteroatom(s) can, however, be used as non-carbon component(s) for carbon composite catalysts, and the resulting heteroatom(s)-doped carbon materials can exhibit improvements in ORR and OER performance. Heteroatom(s)-doped carbon composites can also create more conductive pathways and more active sites for ORR and OER. Importantly, the observed interactions between different heteroatom dopants can also contribute significantly to electrocatalytic activities for ORR and OER. Other material components such as oxides and metals can have more effective influences on the electrocatalytic activity and cycling performance of carbon-composite catalyst MABs. In particular, perovskite oxides exhibit bifunctionality for catalytic ORR and OER in alkaline solutions. To solve issues of carbon corrosion and oxidation in MABs, novel strategies such as carbon-composited ternary bifunctional catalysts have shown promising effects on the improvement of catalytic performances. Compared with individual components, these ternary and/or trinary composite catalysts offer improved catalytic performances and strong resistances to carbon corrosion in MABs.

9.2 Challenges

In recent years, considerable efforts have been concentrated on the development of carbon-composited bifunctional catalysts. Several major technological challenges are still present, however, in the development of commercial MABs: (1) insufficient electrocatalytic activities for both ORR and OER at the air-electrode, leading to low energy/power density and efficiency of MABs; (2) insufficient stability/durability of bifunctional air-electrode catalysts due to low resistances to electrochemical corrosion, resulting in degradation of MAB performance; (3) insufficient strategies for catalyst design, starting material selection, scalable synthesis and catalyst performance optimization; (4) unoptimized MAB electrode/cell design and fabrication; and (5) insufficient fundamental understanding of catalyst interaction, synergy and bifunctionality mechanisms as well as MAB electrode/cell design and fabrication. Overall, the immature capability for bifunctional catalyst optimization and scale-up production with cost-effective approaches for MAB air electrodes is a major hindrance and the understanding of fundamentals is highly useful for material selection and optimization of catalyst/electrode designs.

9.3 Proposed Future Research Directions

To overcome these technical challenges, several future research directions can be proposed as follows for the fabrication of next-generation carbon-composited bifunctional catalysts for MAB air electrodes:

1. Improving the catalytic activity and stability/durability of carbon-composited bifunctional catalysts for MAB air electrodes by developing novel methodologies for catalyst design/synthesis/fabrication to obtain optimal porous structures with optimal pore size and distribution as well as surface area. In such morphology-controlled

synthesis strategies, the recommended pores should be mesopores and macropores, not micropores.

2. Establishing a deeper fundamental understanding of catalytic mechanisms for bifunctional composite catalysts used in different types of MABs through both experimental and theoretical studies. It is necessary to understand the close relationship between the bifunctional catalytic mechanisms of ORR/OER and the electronic structure/composition of catalysts using a combination of molecular/atomic modeling and experimental characterization, allowing for further improvements to catalytic performances of ORR and OER in MABs.
3. Developing novel synthesis approaches with low-cost and/or green materials to effectively fabricate high-performing and cost-effective bifunctional composite catalysts for MAB air electrodes. As an example, biomasses consisting of natural polymers (e.g., cellulose, lignin, and hemicellulose) have been used as starting materials to produce biomass-derived carbons and their composites for advanced bifunctional catalysts.
4. Developing doping strategies to produce doped carbon-composited bifunctional catalysts for MABs. This is because doped carbon materials possess active synergistic interactions between the dopant(s) and carbon in which the synergistic interactions can be designed to improve both electrocatalytic activity and stability/durability.

These critical research directions and their associated strategies must be integrated to develop comprehensive and effective approaches for the design and synthesis of successful bifunctional composite catalysts for MAB air electrodes.

Acknowledgements The authors would like to acknowledge the contributions made by Prof. Anna Ignaszak's group in the Department of Chemistry at the University of New Brunswick.

Compliance with Ethical Standards

Conflict of interest The authors declare that they have no conflict of interests.

References

1. Rahman, M.A., Wang, X., Wen, C.: High energy density metal–air batteries: a review. J. Electrochem. Soc. **160**, A1759–A1771 (2013)
2. Li, Y., Dai, H.: Recent advances in zinc–air batteries. Chem. Soc. Rev. **43**, 5257–5275 (2014)
3. Bagotsky, V.S., Skundin, A.M., Volfkovich, Y.M.: Electrochemical Power Sources: Batteries, Fuel Cells, and Supercapacitors. Wiley, Hoboken (2015)
4. Chen, F.Y., Chen, J.: Metal–air batteries: from oxygen reduction electrochemistry to cathode catalysts. Chem. Soc. Rev. **41**, 2172–2192 (2012)
5. Cao, R., Lee, J.S., Liu, M., et al.: Recent progress in non-precious catalysts for metal–air batteries. Adv. Energy. Mater. **2**, 816–829 (2012)
6. Shao, Y., Park, S., Xiao, J., et al.: Electrocatalysts for nonaqueous lithium–air batteries: status, challenges, and perspective. ACS Catal. **2**, 844–857 (2012)
7. Fujiwara, N., Yao, M., Siroma, Z., et al.: Reversible air electrodes integrated with an anion-exchange membrane for secondary air batteries. J. Power Sources **196**, 808–813 (2011)
8. Lu, Y.C., Xu, Z., Gasteiger, H.A., et al.: Platinum-gold nanoparticles: a highly active bifunctional electrocatalyst for rechargeable lithium–air batteries. J. Am. Chem. Soc. **132**, 12170–12171 (2010)
9. Gorlin, Y., Jaramillo, T.F.: A bifunctional nonprecious metal catalyst for oxygen reduction and water oxidation. J. Am. Chem. Soc. **132**, 13612–13614 (2010)
10. Lee, Y., Suntivich, J., May, K.J., et al.: Synthesis and activities of rutile IrO_2 and RuO_2 nanoparticles for oxygen evolution in acid and alkaline solutions. J. Phys. Chem. Lett. **3**, 399–404 (2012)
11. Velraj, S., Zhu, J.H.: Cycle life limit of carbon-based electrodes for rechargeable metal–air battery application. J. Electroanal. Chem. **736**, 76–82 (2015)
12. Sun, B., Wang, B., Su, D., et al.: Graphene nanosheets as cathode catalysts for lithium–air batteries with an enhanced electrochemical performance. Carbon **50**, 727–733 (2012)
13. Wang, Y.J., Fang, B., Li, H., et al.: Progress in modified carbon support materials for Pt and Pt-alloy cathode catalysts in polymer electrolyte membrane fuel cells. Prog. Mater Sci. **82**, 445–498 (2016)
14. Liu, Y., Wu, P.: Graphene quantum dot hybrids as efficient metal-free electrocatalyst for the oxygen reduction reaction. ACS Appl. Mater. Interfaces **5**, 3362–3369 (2013)
15. Li, Y., Zhao, Y., Cheng, H., et al.: Nitrogen-doped graphene quantum dots with oxygen-rich functional groups. J. Am. Chem. Soc. **134**, 15–18 (2012)
16. Wang, M., Fang, Z., Zhang, K., et al.: Synergistically enhanced activity of graphene quantum dots/graphene hydrogel composites: a novel all-carbon hybrid electrocatalyst for metal/air batteries. Nanoscale **8**, 11398–11402 (2016)
17. Peng, J., Gao, W., Gupta, B.K., et al.: Graphene quantum dots derived from carbon fibers. Nano Lett. **12**, 844–849 (2012)
18. Yu, D., Zhang, Q., Dai, L.: Highly efficient metal-free growth of nitrogen-doped single-walled carbon nanotubes on plasma-etched substrates for oxygen reduction. J. Am. Chem. Soc. **132**, 15127–15129 (2010)
19. Luo, G., Huang, S.T., Zhao, N., et al.: A super high discharge capacity induced by a synergetic effect between high-surface-area carbons and a carbon paper current collector in a lithium–oxygen battery. Chin. Phys. B **24**, 088102 (2015)
20. Song, M.J., Shin, M.W.: Fabrication and characterization of carbon nanofiber@mesoporous carbon core–shell composite for the Li–air battery. Appl. Surf. Sci. **320**, 435–440 (2014)
21. Zhao, Z., Li, M., Zhang, L., et al.: Design principles for heteroatom-doped carbon nanomaterials as highly efficient catalysts for fuel cells and metal–air batteries. Adv. Mater. **27**, 6834–6840 (2015)
22. Ren, X., Wang, B., Zhu, J., et al.: The doping effect on the catalytic activity of graphene for oxygen evolution reaction in a lithium–air battery: a first-principles study. Phys. Chem. Chem. Phys. **17**, 14605–14612 (2015)

23. Li, L., Manthiram, A.: O- and N-doped carbon nanowebs as metal-free catalysts for hybrid Li–air batteries. Adv. Energy Mater. **4**, 1301795 (2014)
24. Lin, X., Lu, X., Huang, T., et al.: Binder-free nitrogen-doped carbon nanotubes electrodes for lithium–oxygen batteries. J. Power Sources **242**, 855–859 (2013)
25. Wang, Z., Xiong, X., Qie, L., et al.: High-performance lithium storage in nitrogen-enriched carbon nanofiber webs derived from polypyrrole. Electrochim. Acta **106**, 320–326 (2013)
26. Li, H., Kang, W., Wang, L., et al.: Synthesis of three-dimensional flowerlike nitrogen-doped carbons by a copyrolysis route and the effect of nitrogen species on the electrocatalytic activity in oxygen reduction reaction. Carbon **54**, 249–257 (2013)
27. Mi, R., Liu, H., Wang, H., et al.: Effects of nitrogen-doped carbon nanotubes on the discharge performance of Li–air batteries. Carbon **67**, 744–752 (2014)
28. Shin, W.H., Jeong, H.M., Kim, B.G., et al.: Nitrogen-doped multiwall carbon nanotubes for lithium storage with extremely high capacity. Nano Lett. **12**, 2283–2288 (2012)
29. Antonietti, M., Fechler, N., Fellinger, T.P.: Carbon aerogels and monoliths: control of porosity and nanoarchitecture via sol–gel routes. Chem. Mater. **26**, 196–210 (2014)
30. Sakaushi, K., Fellinger, T.P., Antonietti, M.: Bifunctional metal-free catalysis of mesoporous noble carbons for oxygen reduction and evolution reactions. Chemsuschem **8**, 1156–1160 (2015)
31. Men, Y., Siebenbürger, M., Qiu, X.: Low fractions of ionic liquid or poly(ionic liquid) can activate polysaccharide biomass into shaped, flexible and fire-retardant porous carbons. J. Mater. Chem. A **1**, 11887–11893 (2013)
32. Balach, J., Wu, H., Polzer, F.: Poly(ionic liquid)-derived nitrogen-doped hollow carbon spheres: synthesis and loading with Fe_2O_3 for high-performance lithium ion batteries. RSC Adv. **3**, 7979–7986 (2013)
33. Liu, Z., Zhang, G., Lu, Z.: One-step scalable preparation of N-doped nanoporous carbon as a high-performance electrocatalyst for the oxygen reduction reaction. Nano Res. **6**, 293–301 (2013)
34. Hadidi, L., Davari, E., Lqbal, M.: Spherical nitrogen-doped hollow mesoporous carbon as an efficient bifunctional electrocatalyst for Zn–air batteries. Nanoscale **7**, 20547–20556 (2015)
35. Cong, K., Radtke, M., Stumpf, S.: Electrochemical stability of the polymer-derived nitrogen-doped carbon: an elusive goal? Mater. Renew Sustain Energy **4**, 5 (2015)
36. Ma, J.L., Zhang, X.B.: Optimized nitrogen-doped carbon with a hierarchically porous structure as a highly efficient cathode for Na–O_2 batteries. J. Mater. Chem. A **4**, 10008–10013 (2016)
37. Long, G., Wan, K., Liu, M., et al.: Effect of pyrolysis conditions on nitrogen-doped ordered mesoporous carbon electrocatalysts. Chin. J. Catal. **36**, 1197–1204 (2015)
38. Eisenberg, D., Stroek, W., Geels, N.J., et al.: A simple synthesis of an N-doped carbon ORR catalyst: hierarchical micro/meso/macro porosity and graphitic shells. Chem. Eur. J. **22**, 501–505 (2016)
39. Trogadas, P., Ramani, V., Strasser, P., et al.: Hierarchically structured nanomaterials for electrochemical energy conversion. Angew. Chem. Int. Ed. **55**, 122–148 (2016)
40. Zhao, B., Collinson, M.M.: Well-defined hierarchical templates for multimodal porous material fabrication. Chem. Mater. **22**, 4312–4319 (2010)
41. Wang, M., Lai, Y., Fang, J., et al.: N-doped porous carbon derived from biomass as an advanced electrocatalyst for aqueous aluminum/air battery. Int. J. Hydrogen Energy **40**, 16230–16237 (2015)
42. Zeng, X., Leng, L., Liu, F., et al.: Enhanced Li–O_2 battery performance, using graphene-like nori-derived carbon as the cathode and adding LiI in the electrolyte as a promoter. Electrochim. Acta **200**, 231–238 (2016)
43. Wang, L., Yin, F., Yao, C.: N-doped graphene as a bifunctional electrocatalyst for oxygen reduction and oxygen evolution reactions in an alkaline electrolyte. Inter. J. Hydrog. Energ. **39**, 15913–15919 (2014)
44. Zhao, C., Yu, C., Liu, S., et al.: 3D porous N-doped graphene frameworks made of interconnected nanocages for ultrahigh-rate and long-life Li–O_2 batteries. Adv. Funct. Mater. **25**, 6913–6920 (2015)
45. He, M., Zhang, P., Liu, L., et al.: Hierarchical porous nitrogen doped three-dimensional graphene as a free-standing cathode for rechargeable lithium–oxygen batteries. Electrochim. Acta **191**, 90–97 (2016)
46. Yan, H.J., Xu, B., Shi, S.Q., et al.: First-principles study of the oxygen adsorption and dissociation on graphene and nitrogen doped graphene for Li–air batteries. J. Appl. Phys. **112**, 104316 (2012)
47. Zhang, Z., Bao, J., He, C., et al.: Hierarchical carbon-nitrogen architectures with both mesopores and macrochannels as excellent cathodes for rechargeable Li–O_2 batteries. Adv. Funct. Mater. **24**, 6826–6833 (2014)
48. Yadav, R.M., Wu, J., Kochandra, R., et al.: Carbon nitrogen nanotubes as efficient bifunctional electrocatalysts for oxygen reduction and evolution reactions. ACS Appl. Mater. Interfaces **7**, 11991–12000 (2015)
49. Li, Y., Wang, J., Li, X., et al.: Nitrogen-doped carbon nanotubes as cathode for lithium–air batteries. Electrochem. Commun. **13**, 668–672 (2011)
50. Liu, Q., Wang, Y., Dai, L., et al.: Scalable fabrication of nanoporous carbon fiber films as bifunctional catalytic electrodes for flexible Zn–air batteries. Adv. Mater. **28**, 3000–3006 (2016)
51. Shui, J., Du, F., Xue, C., et al.: Vertically aligned N-doped coral-like carbon fiber arrays as efficient air electrodes for high-performance nonaqueous Li–O_2 batteries. ACS Nano **8**, 3015–3022 (2014)
52. Park, G.S., Lee, J.S., Kim, S.T.: Porous nitrogen doped carbon fiber with churros morphology derived from electrospun bicomponent polymer as highly efficient electrocatalyst for Zn–air batteries. J. Power Sources **243**, 267–273 (2013)
53. Liu, J., Wang, Z., Zhu, J.: Binder-free nitrogen-doped carbon paper electrodes derived from polypyrrole/cellulose composite for Li–O_2 batteries. J. Power Sources **306**, 559–566 (2016)
54. Lu, H.J., Li, Y., Zhang, L.Q., et al.: Synthesis of B-doped hollow carbon spheres as efficient non-metal catalyst for oxygen reduction reaction. RSC Adv. **5**, 52126–52131 (2015)
55. Zheng, Y., Jiao, Y., Jaroniec, M., et al.: Nanostructured metal-free electrochemical catalysts for highly efficient oxygen reduction. Small **8**, 3550–3566 (2012)
56. Yang, L.J., Jiang, S.J., Zhao, Y., et al.: Boron-doped carbon nanotubes as metal-free electrocatalysts for the oxygen reduction reaction. Angew. Chem. Int. Ed. **50**, 7132–7135 (2011)
57. Shu, C., Lin, Y., Zhang, B., et al.: Mesoporous boron-doped onion-like carbon as long-life oxygen electrode for sodium–oxygen batteries. J. Mater. Chem. A **4**, 6610–6619 (2016)
58. Su, J., Cao, X., Wu, J., et al.: One-pot synthesis of boron-doped ordered mesoporous carbon as efficient electrocatalysts for the oxygen reduction reaction. RSC Adv. **6**, 24728–24737 (2016)
59. Lin, Y.M., Su, D.S.: Fabrication of nitrogen-modified annealed nanodiamond with improved catalytic activity. ACS Nano **8**, 7823–7833 (2014)
60. Wang, R., Sun, X., Zhang, B., et al.: Hybrid nanocarbon as a catalyst for direct dehydrogenation of propane: formation of an active and selective core–shell sp^2/sp^3 nanocomposite structure. Chem. Eur. J. **20**, 6324–6331 (2014)

61. Cermignani, W., Paulson, T.E., Onneby, C., et al.: Synthesis and characterization of boron-doped carbons. Carbon **33**, 367–374 (1995)
62. Lin, Y., Zhu, Y., Zhang, B., et al.: Boron-doped onion-like carbon with enriched substitutional boron: the relationship between electronic properties and catalytic performance. J. Mater. Chem. A **3**, 21805–21814 (2015)
63. Wu, J., Yang, Z., Sun, Q., et al.: Synthesis and electrocatalytic activity of phosphorus-doped carbon xerogel for oxygen reduction. Electrochim. Acta **127**, 53–60 (2014)
64. Zhu, Y.P., Liu, Y., Liu, Y.P., et al.: Direct synthesis of phosphorus-doped mesoporous carbon materials for efficient electrocatalytic oxygen reduction. ChemCatChem **7**, 2903–2909 (2015)
65. Wu, J., Yang, Z., Li, X., et al.: Phosphorus-doped porous carbons as efficient electrocatalysts for oxygen reduction. J. Mater. Chem. A **1**, 9889–9896 (2013)
66. Dake, L.S., Baer, D.R., Friedrich, D.M.: Auger parameter measurements of phosphorus compounds for characterization of phosphazenes. J. Vac. Sci. Technol. A **7**, 1634 (1989)
67. Paraknowitsch, J.P., Zhang, Y.J., Wienert, B., et al.: Nitrogen- and phosphorus-co-doped carbons with tunable enhanced surface areas promoted by the doping additives. Chem. Commun. **49**, 1208–1210 (2013)
68. Li, R., Wei, Z., Gou, X., et al.: Phosphorus-doped graphene nanosheets as efficient metal-free oxygen reduction electrocatalysts. RSC Adv. **3**, 9978–9984 (2013)
69. Zhang, S., Cai, Y., He, H., et al.: Heteroatom doped graphdiyne as efficient metal-free electrocatalyst for oxygen reduction reaction in alkaline medium. J. Mater. Chem. A **4**, 4738–4744 (2016)
70. Choi, C.H., Park, S.H., Woo, S.I.: Binary and ternary doping of nitrogen, boron, and phosphorus into carbon for enhancing electrochemical oxygen reduction activity. ACS Nano **6**, 7084–7091 (2012)
71. Wang, S., Lyyamperumal, E., Roy, A., et al.: Vertically aligned BCN nanotubes as efficient metal-free electrocatalysts for the oxygen reduction reaction: a synergetic effect by Co-doping with boron and nitrogen. Angew. Chem. Int. Ed. **50**, 11756–11760 (2011)
72. Liang, J., Jiao, Y., Jaroniec, M., et al.: Sulfur and nitrogen dual-doped mesoporous graphene electrocatalyst for oxygen reduction with synergistically enhanced performance. Angew. Chem. Int. Ed. **51**, 11496–11500 (2012)
73. Jiao, Y., Zheng, Y., Jaroniec, M., et al.: Origin of the electrocatalytic oxygen reduction activity of graphene-based catalysts: a roadmap to achieve the best performance. J. Am. Chem. Soc. **136**, 4394–4403 (2014)
74. Zhang, J., Zhao, Z., Xia, Z., et al.: A metal-free bifunctional electrocatalyst for oxygen reduction and oxygen evolution reactions. Nat. Nanotechnol. **10**, 444–452 (2015)
75. Gorham, J., Torres, J., Wolfe, G., et al.: Surface reactions of molecular and atomic oxygen with carbon phosphide films. J. Phys. Chem. B **109**, 20379–20386 (2005)
76. Bao, X., Nie, X., Deak, D.V., et al.: A first-principles study of the role of quaternary-N doping on the oxygen reduction reaction activity and selectivity of graphene edge sites. Top. Catal. **56**, 1623–1633 (2013)
77. Song, L., Liu, Z., Reddy, A.L.M., et al.: Binary and ternary atomic layers built from carbon, boron, and nitrogen. Adv. Mater. **24**, 4878–4895 (2012)
78. Zheng, Y., Jiao, Y., Ge, L., et al.: Two-step boron and nitrogen doping in graphene for enhanced synergistic catalysis. Angew. Chem. Int. Ed. **52**, 3110–3116 (2013)
79. Pels, J.R., Kapteijin, F., Moulijn, J.A., et al.: Evolution of nitrogen functionalities in carbonaceous materials during pyrolysis. Carbon **33**, 1641–1653 (1995)
80. Matsumoto, M., Yamada, M., Watanabe, N.: Reversible 1,4-cycloaddition of singlet oxygen to N-substituted 2-pyridones: 1,4-endoperoxide as a versatile chemical source of singlet oxygen. Chem. Commun. **36**, 483–485 (2005)
81. Wu, M., Qiao, J., Li, K., et al.: A large-scale synthesis of heteroatom (N and S) co-doped hierarchically porous carbon (HPC) derived from polyquaternium for superior oxygen reduction reactivity. Green Chem. **18**, 2699–2709 (2016)
82. Yazdi, A.Z., Roberts, E.P.L., Sundararaj, U.: Nitrogen/sulfur co-doped helical graphene nanoribbons for efficient oxygen reduction in alkaline and acidic electrolytes. Carbon **100**, 99–108 (2016)
83. Qu, K., Zheng, Y., Dai, S., et al.: Graphene oxide-polydopamine derived N, S-codoped carbon nanosheets as superior bifunctional electrocatalyst for oxygen reduction and evolution. Nano Energy **19**, 373–381 (2016)
84. Pettersson, J., Ramsey, B., Harrison, D.: A review of the latest developments in electrodes for unitized regenerative polymer electrolyte fuel cells. J. Power Sources **157**, 28–34 (2006)
85. Ikezawa, A., Miyazaki, K., Fukutsuka, T., et al.: Investigation of electrochemically active regions in bifunctional air electrodes using partially immersed platinum electrodes. J. Electrochem. Soc. **162**, A1646–A1653 (2015)
86. Wang, L., Ara, M., Wadumesthrige, K., et al.: Graphene nanosheet supported bifunctional catalyst for high cycle life Li–air batteries. J. Power Sources **234**, 8–15 (2013)
87. Yin, J., Fang, B., Luo, J., et al.: Nanoscale alloying effect of gold-platinum nanoparticles as cathode catalysts on the performance of a rechargeable lithium–oxygen battery. Nanotechnology **23**, 305404 (2012)
88. Terashima, C., Iwai, Y., Cho, S.P., et al.: Solution plasma sputtering processes for the synthesis of PtAu/C catalysts for Li–air batteries. Int. J. Electrochem. Sci. **8**, 5407–5420 (2013)
89. Su, D., Kim, H.S., Kim, W.S., et al.: A study of PtxCoy alloy nanoparticles as cathode catalysts for lithium–air batteries with improved catalytic activity. J. Power Sources **244**, 488–493 (2013)
90. Zhang, Y., Wu, X., Fu, Y., et al.: Carbon aerogel supported Pt–Zn catalyst and its oxygen reduction catalytic performance in magnesium–air batteries. J. Mater. Res. **29**, 2863–2870 (2014)
91. Ko, B.K., Kim, M.K., Kim, S.H., et al.: Synthesis and electrocatalytic properties of various metals supported on carbon for lithium–air battery. J. Mol. Catal. A: Chem. **379**, 9–14 (2013)
92. Ke, F.S., Solomon, B.C., Ma, S.G., et al.: Metal-carbon nanocomposites as the oxygen electrode for rechargeable lithium–air batteries. Electrochim. Acta **85**, 444–449 (2012)
93. Zhou, W., Cheng, Y., Yang, X., et al.: Iridium incorporated into deoxygenated hierarchical graphene as a high-performance cathode for rechargeable Li–O_2 batteries. J. Mater. Chem. A **3**, 14556–14561 (2015)
94. Ottakam Thotiyl, M.M., Freunberger, S.A., Peng, Z.Q., et al.: The carbon electrode in nonaqueous Li–O_2 cells. J. Am. Chem. Soc. **135**, 494–500 (2013)
95. Itkis, D.M., Semenenko, D.A., Kataev, E.Y., et al.: Reactivity of carbon in lithium–oxygen battery positive electrodes. Nano Lett. **13**, 4697–4701 (2013)
96. Tong, S., Zheng, M., Lu, Y., et al.: Binder-free carbonized bacterial cellulose-supported ruthenium nanoparticles for Li–O_2 batteries. Chem. Commun. **51**, 7302–7304 (2015)
97. Ma, S., Wu, Y., Wang, J., et al.: Reversibility of noble metal-catalyzed aprotic Li–O_2 batteries. Nano Lett. **15**, 8084–8090 (2015)
98. Alegre, C., Modica, E., Lo Vecchio, C., et al.: Carbon nanofibers as advanced Pd catalyst supports for the air electrode of alkaline metal–air batteries. ChemPlusChem **80**, 1384–1388 (2015)

99. McKerracher, R.D., Alegre, C., Baglio, V., et al.: A nanostructured bifunctional Pt/C gas-diffusion electrode for metal–air batteries. Electrochim. Acta **174**, 508–515 (2015)
100. Cheng, H., Scott, K.: Selection of oxygen reduction catalyst for rechargeable lithium–air batteries-metal or oxide? Appl. Catal. B Environ. **108–109**, 140–151 (2011)
101. Marinaro, M., Riek, U., Eswara Moorthy, S.K., et al.: Au-coated carbon cathodes for improved reduction and evolution kinetics in aprotic Li–O_2 batteries. Electrochem. Commun. **37**, 53–56 (2013)
102. Wang, T., Kaempgen, M., Nopphawan, P., et al.: Silver nanoparticle-decorated carbon nanotubes as bifunctional gas-diffusion electrodes for zinc–air batteries. J. Power Sources **195**, 4350–4355 (2011)
103. Cui, Z., Chen, H., Zhao, M., et al.: High-performance Pd_3Pb intermetallic catalyst for electrochemical oxygen reduction. Nano Lett. **16**, 2560–2566 (2016)
104. Li, J., Zhao, Y., Zou, M., et al.: An effective integrated design for enhanced cathodes of Ni foam-supported Pt/carbon nanotubes for Li–O_2 batteries. ACS Appl. Mater. Interfaces **6**, 12479–12485 (2014)
105. Yu, R., Fan, W., Guo, X., et al.: Highly ordered and ultralong carbon nanotube arrays as air cathodes for high-energy-efficiency Li–oxygen batteries. J. Power Sources **306**, 402–407 (2016)
106. Su, L., Hei, J., Wu, X., et al.: Highly-dispersed Ni-QDs/mesoporous carbon nanoplates: a universal and commercially applicable approach based on corn straw piths and high capacitive performances. ChemElectroChem **2**, 1897–1902 (2015)
107. Chen, Y., Zhang, Q., Zhang, Z., et al.: Two better than one: cobalt-copper bimetallic yolk-shell nanoparticles supported on graphene as excellent cathode catalyst for Li–O_2 batteries. J. Mater. Chem. A **3**, 17874–17879 (2015)
108. Xu, J.J., Wang, Z.L., Xu, D., et al.: Tailoring deposition and morphology of discharge products towards high-rate and long-life lithium–oxygen batteries. Nat. Commun. **4**, 2438 (2013)
109. Xu, J.J., Wang, Z.L., Xu, D., et al.: 3D ordered macroporous $LaFeO_3$ as efficient electrocatalyst for Li–O_2 batteries with enhanced rate capability and cyclic performance. Energy Environ. Sci. **7**, 2213–2219 (2014)
110. Kwak, W.J., Kang, T.G., Sun, Y.K., et al.: Iron–cobalt bimetal decorated carbon nanotubes as cost-effective cathode catalysts for Li–O_2 batteries. J. Mater. Chem. A **4**, 7020–7026 (2016)
111. Huang, J., Zhang, B., Xie, Y.Y., et al.: Electrospun graphitic carbon nanofibers with in situ encapsulated Co–Ni nanoparticles as freestanding electrodes for Li–O_2 batteries. Carbon **100**, 329–336 (2016)
112. Ren, X., Zhang, S.S., Tran, D.T., et al.: Oxygen reduction reaction catalyst on lithium/air discharge performance. J. Mater. Chem. **21**, 10118–10125 (2011)
113. Li, J., Zou, M., Chen, L., et al.: An efficient bifunctional catalyst of Fe/Fe_3C carbon nanofibers for rechargeable Li–O_2 batteries. J. Mater. Chem. A **2**, 10634–10638 (2014)
114. Wang, X., Liu, X., Tong, C.J., et al.: An electron injection promoted highly efficient electrocatalyst of $FeNi_3$@GR@Fe–NiOOH for oxygen evolution and rechargeable metal–air batteries. J. Mater. Chem. A **4**, 7762–7771 (2016)
115. Wang, Q., Zhou, D., Yu, H., et al.: NiFe layered double-hydroxide and cobalt-carbon composite as a high-performance electrocatalyst for bifunctional oxygen electrode. J. Electrochem. Soc. **162**, A2362–A2366 (2015)
116. Li, B., Chen, Y., Ge, X., et al.: Mussel-inspired one-pot synthesis of transition metal and nitrogen co-doped carbon (M/N–C) as efficient oxygen catalysts for Zn–air batteries. Nanoscale **8**, 5067–5075 (2016)
117. Wu, M., Tang, Q., Dong, F., et al.: The design of Fe, N-doped hierarchically porous carbons as highly active and durable electrocatalysts for a Zn–air battery. Phys. Chem. Chem. Phys. **18**, 18665–18669 (2016)
118. Wang, J., Wu, H., Gao, D., et al.: High-density iron nanoparticles encapsulated within nitrogen-doped carbon nanoshell as efficient oxygen electrocatalyst for zinc–air battery. Nano Energy **13**, 387–396 (2015)
119. Oh, D., Qi, J., Han, B., et al.: M13 virus-directed synthesis of nanostructured metal oxides for lithium–oxygen batteries. Nano Lett. **14**, 4837–4845 (2014)
120. Esswein, A.J., McMurdo, M.J., Ross, P.N., et al.: Size-dependent activity of Co_3O_4 nanoparticle anodes for alkaline water electrolysis. J. Phys. Chem. C **113**, 15068–15072 (2009)
121. Koza, J.A., He, Z., Miller, A.S., et al.: Electrodeposition of crystalline Co_3O_4—a catalyst for the oxygen evolution reaction. Chem. Mater. **24**, 3567–3573 (2012)
122. Li, Q., Cao, R., Cho, J., et al.: Nanostructured carbon-based cathode for nonaqueous lithium–oxygen batteries. Phys. Chem. Chem. Phys. **16**, 13568–13582 (2014)
123. Li, Q., Cao, R., Cho, J., et al.: Nanocarbon electrocatalysts for oxygen reduction in alkaline media for advanced energy conversion and storage. Adv. Energy Mater. **4**, 1301415 (2014)
124. Gupta, S., Kellogg, W., Xu, H., et al.: Bifunctional perovskite oxide catalysts for oxygen reduction and evolution in alkaline media. Chem. Asian J. **11**, 10–21 (2016)
125. Suntivich, J., Gasteiger, H.A., Yabuuchi, N., et al.: Design principles for oxygen-reduction activity on perovskite oxide catalysts for fuel cells and metal–air batteries. Nat. Chem. **3**, 647 (2011)
126. Suntivich, J., May, K.J., Gasteiger, A., et al.: A perovskite oxide optimized for oxygen evolution catalysis from molecular orbital principles. Science **334**, 1383–1385 (2011)
127. Xu, Y., Tsou, A., Fu, Y., et al.: Carbon-coated perovskite $BaMnO_3$ porous nanorods with enhanced electrocatalytic properties for oxygen reduction and oxygen evolution. Electrochim. Acta **174**, 551–556 (2015)
128. Nishio, K., Molla, S., Okugaki, T., et al.: Effects of carbon on oxygen reduction and evolution reactions of gas-diffusion air electrodes based on perovskite-type oxides. J. Power Sources **298**, 236–240 (2015)
129. Gupta, S., Kellogg, W., Xu, H., et al.: Bifunctional perovskite oxide catalysts for oxygen reduction and evolution in alkaline media. Chem. Asian J. **11**, 10–21 (2016)
130. Velraj, S., Zhu, J.H.: $Sr_{0.5}Sm_{0.5}CoO_{3-\delta}$—a new bi-functional catalyst for rechargeable metal–air battery applications. J. Power Sources **227**, 48–52 (2013)
131. Yuasa, M., Matsuyoshi, T., Kida, T., et al.: Discharge/charge characteristic of Li–air cells using carbon-supported $LaMn_{0.6}Fe_{0.4}O_3$ as an electrocatalyst. J. Power Sources **242**, 216–221 (2013)
132. Ross, P.N., Sokol, H.: The corrosion of carbon black anodes in alkaline electrolyte. I. acetylene black and the effect of cobalt catalyzation. J. Electrochem. Soc. **131**, 1742–1750 (1984)
133. Chung, K.B., Shin, J.K., Jang, T.Y.: Preparation and analyses of MnO_2/carbon composites for rechargeable lithium–air battery. Rev. Adv. Mater. Sci. **28**, 54–58 (2011)
134. Yuasa, M., Tachibana, N., Shimanoe, K.: Oxygen reduction activity of carbon-supported $La_{1-x}Ca_xMn_{1-y}Fe_yO_3$ nanoparticles. Chem. Mater. **25**, 3072–3079 (2013)
135. Yuasa, M., Shimanoe, K., Teraoka, Y., et al.: High-performance oxygen reduction catalyst using carbon-supported La-Mn-based perovskite-type oxide. Electrochem. Solid-State Lett. **14**, A67–A69 (2011)
136. Park, M.S., Kim, J., Kim, K.J., et al.: Porous nanoarchitectures of spinel-type transition metal oxides for electrochemical energy storage systems. Phys. Chem. Chem. Phys. **17**, 30963–30977 (2015)

137. Li, P., Ma, R., Zhou, Y., et al.: In situ growth of spinel $CoFe_2O_4$ nanoparticles on rod-like ordered mesoporous carbon for bifunctional electrocatalysis of both oxygen reduction and oxygen evolution. J. Mater. Chem. A **3**, 15598–15606 (2015)
138. Yan, W., Bian, W., Jin, C., et al.: An efficient bi-functional electrocatalyst based on strongly coupled $CoFe_2O_4$/carbon nanotubes hybrid for oxygen reduction and oxygen evolution. Electrochim. Acta **177**, 65–72 (2015)
139. Lee, D.U., Kim, B.J., Chen, Z.: One-pot synthesis of a mesoporous $NiCo_2O_4$ nanoplatelet and graphene hybrid and its oxygen reduction and evolution activities as an efficient bi-functional electrocatalyst. J. Mater. Chem. A **1**, 4754–4762 (2013)
140. Bian, W., Yang, Z., Strasser, P., et al.: A $CoFe_2O_4$/graphene nanohybrid as an efficient bi-functional electrocatalyst for oxygen reduction and oxygen evolution. J. Power Sources **250**, 196–203 (2014)
141. Liu, S., Bian, W., Yang, Z., et al.: A facile synthesis of $CoFe_2O_4$/biocarbon nanocomposites as efficient bi-functional electrocatalysts for the oxygen reduction and oxygen evolution reaction. J. Mater. Chem. A **2**, 18012–18017 (2014)
142. Liu, Y., Higgins, D.C., Wu, J., et al.: Cubic spinel cobalt oxide/multi-walled carbon nanotube composites as an efficient bifunctional electrocatalyst for oxygen reaction. Electrochem. Commun. **34**, 125–129 (2013)
143. Jiang, Q., Liang, L.H., Zhao, D.S.: Lattice contraction and surface stress of fcc nanocrystals. J. Phys. Chem. B **105**, 6275–6277 (2001)
144. Lopes, I., El Hassan, N., Guerba, H., et al.: Size-induced structural modifications affecting Co_3O_4 nanoparticles patterned in SBA-15 silicas. Chem. Mater. **18**, 5826–5828 (2006)
145. Gao, R., Li, Z., Zhang, X., et al.: Carbon-dotted defective CoO with oxygen vacancies: a synergetic deign of bifunctional cathode catalyst for Li–O_2 batteries. ACS Catal. **6**, 400–406 (2016)
146. Huang, B.W., Li, L., He, Y.J., et al.: Enhanced electrochemical performance of nanofibrous CoO/CNF cathode catalyst for Li–O_2 batteries. Electrochim. Acta **137**, 183–189 (2014)
147. Salehi, M., Shariatinia, Z.: An optimization of MnO_2 amount in CNT–MnO_2 nanocomposite as a high rate cathode catalyst for the rechargeable Li–O_2 batteries. Electrochim. Acta **188**, 428–440 (2016)
148. Sumboja, A., Ge, X., Thomas Goh, F.W., et al.: Manganese oxide catalyst grown on carbon paper as an air cathode for high-performance rechargeable zinc–air batteries. ChemPlusChem **80**, 1341–1346 (2015)
149. Tan, P., Shyy, W., Zhao, T.S., et al.: A RuO_2 nanoparticle-decorated buckypaper cathode for non-aqueous lithium–oxygen batteries. J. Mater. Chem. A **3**, 19042–19049 (2015)
150. Jung, H.G., Jeong, Y.S., Park, J.B., et al.: Ruthenium-based electrocatalysts supported on reduced graphene oxide for lithium–air batteries. ACS Nano **7**, 3532–3539 (2013)
151. Zhang, X., Xiao, Q., Zhang, Y., et al.: La_2O_3 doped carbonaceous microspheres: a novel bifunctional electrocatalyst for oxygen reduction and evolution reactions with ultrahigh mass activity. J. Phys. Chem. C **118**, 20229–20237 (2014)
152. Ahn, C.H., Kalubarme, R.S., Kim, Y.H., et al.: Graphene/doped ceria nano-blend for catalytic oxygen reduction in non-aqueous lithium–oxygen batteries. Electrochim. Acta **117**, 18–25 (2014)
153. Liu, X., Park, M., Kim, M.G., et al.: High-performance non-spinel cobalt-manganese mixed oxide-based bifunctional electrocatalysts for rechargeable zinc–air batteries. Nano Energy **20**, 315–325 (2016)
154. Lu, X., Wang, G., Zhai, T., et al.: Stabilized TiN nanowire arrays for high-performance and flexible supercapacitors. Nano Lett. **12**, 5376–5381 (2012)
155. Li, F., Ohnishi, R., Yamada, Y., et al.: Carbon supported TiN nanoparticles: an efficient bifunctional catalyst for non-aqueous Li–O_2 batteries. Chem. Commun. **49**, 1175–1177 (2013)
156. Laoire, C.O., Mukerjee, S., Abraham, K.M., et al.: Influence of nonaqueous solvents on the electrochemistry of oxygen in the rechargeable lithium–air Battery. J. Phys. Chem. C **114**, 9178–9186 (2010)
157. Laoire, C.O., Mukerjee, S., Abraham, K.M.: Elucidating the mechanism of oxygen reduction for lithium–air battery applications. J. Phys. Chem. C **113**, 20127–20134 (2009)
158. Park, J., Jun, Y.S., Lee, W., et al.: Bimodal mesoporous titanium nitride/carbon microfibers as efficient and stable electrocatalysts for Li–O_2 batteries. Chem. Mater. **25**, 3779–3781 (2013)
159. Lyth, S.M., Nabae, Y., Moriya, S., et al.: Carbon nitride as a nonprecious catalyst for electrochemical oxygen reduction. J. Phys. Chem. C **113**, 20148–20151 (2009)
160. Zhang, L., Su, Z., Jiang, F., et al.: Highly graphitized nitrogen-doped porous carbon nanopolyhedra derived from ZIF-8 nanocrystals as efficient electrocatalysts for oxygen reduction reactions. Nanoscale **6**, 6590–6602 (2014)
161. Zhang, Y., Mori, T., Ye, J., et al.: Phosphorus-doped carbon nitride solid: enhanced electrical conductivity and photocurrent generation. J. Am. Chem. Soc. **132**, 6294–6295 (2010)
162. Fu, X., Hu, X., Yan, Z., et al.: Template-free synthesis of porous graphitic carbon nitride/carbon composite spheres for electrocatalytic oxygen reduction reaction. Chem. Commun. **52**, 1725–1728 (2016)
163. Ma, T.Y., Ran, J., Dai, S., et al.: Phosphorus-doped graphitic carbon nitrides grown in situ on carbon-fiber paper: flexible and reversible oxygen electrodes. Angew. Chem. Int. Ed. **54**, 4646–4650 (2015)
164. Huang, K., Bi, K., Xu, J.C., et al.: Novel graphite-carbon encased tungsten carbide nanocomposites by solid-state reaction and their ORR electrocatalytic performance in alkaline medium. Electrochim. Acta **174**, 172–177 (2015)
165. Koo, B.S., Lee, J.K., Yoon, W.Y.: Improved electrochemical performances of lithium–oxygen batteries with tungsten carbide-coated cathode, Japan. J. Appl. Phys. **54**, 047101 (2015)
166. Luo, W.B., Chou, S.L., Wang, J.Z., et al.: A B_4C nanowire and carbon nanotube composite as a novel bifunctional electrocatalyst for high energy lithium oxygen batteries. J. Mater. Chem. A **3**, 18395–18399 (2015)
167. Werheit, H., Au, T., Schmechel, R., et al.: IR-active phonons and structure elements of isotope-enriched boron carbide. J. Solid State Chem. **154**, 79–86 (2000)
168. Lazzari, R., Vst, N., Besson, J.M., et al.: Atomic structure and vibrational properties of icosahedral B_4C boron carbide. Phys. Rev. Lett. **83**, 3230–3233 (1999)
169. Lyu, Z., Zhang, J., Wang, L., et al.: CoS_2 nanoparticles–graphene hybrid as a cathode catalyst for aprotic Li–O_2 batteries. RSC Adv. **6**, 31739–31743 (2016)
170. Wu, J., Dou, S., Shen, A., et al.: One-step hydrothermal synthesis of $NiCo_2S_4$–*r*GO as an efficient electrocatalyst for the oxygen reduction reaction. J. Mater. Chem. A **2**, 20990–20995 (2014)
171. Chen, W., Lai, Y., Zhang, Z., et al.: β-FeOOH decorated highly porous carbon aerogels composites as a cathode material for rechargeable Li–O_2 batteries. J. Mater. Chem. A **3**, 6447–6454 (2015)
172. Hu, X., Fu, X., Chen, J.: A soil/Vulcan XC-72 hybrid as a highly-effective catalytic cathode for rechargeable Li–O_2 batteries. Inorg. Chem. Front. **2**, 1006–1010 (2015)
173. Lee, C.K., Park, Y.J.: Polyimide-wrapped carbon nanotube electrodes for long cycle Li–air batteries. Chem. Commun. **51**, 1210–1213 (2015)

174. Yoo, E., Zhou, H.: Fe phthalocyanine supported by graphene nanosheet as catalyst in Li–air battery with the hybrid electrolyte. J. Power Sources **244**, 429–434 (2013)
175. Zhai, X., Yang, W., Li, M., et al.: Noncovalent hybrid of $CoMn_2O_4$ spinel nanocrystals and poly(diallyldimethylammonium chloride) functionalized carbon nanotubes as efficient electrocatalyst for oxygen reduction reaction. Carbon **65**, 277–286 (2013)
176. Ma, H., Wang, B.: A bifunctional electrocatalyst α-MnO_2–$LaNiO_3$/carbon nanotube composite for rechargeable zinc–air batteries. RSC Adv. **4**, 46084–46092 (2014)
177. Wu, Q., Jiang, L., Qi, L., et al.: Electrocatalytic performance of Ni modified MnO_x/C composites toward oxygen reduction reaction and their application. Int. J. Hydrogen Energy **39**, 3423–3432 (2014)
178. Li, J., Zou, M., Wen, W., et al.: Spinel MFe_2O_4 (M=Co, Ni) nanoparticles coated on multi-walled carbon nanotubes as electrocatalysts for Li–O_2 batteries. J. Mater. Chem. A **2**, 10257–10262 (2014)
179. Prabu, M., Ramakrishnan, P., Nara, H., et al.: Zinc–air battery: understanding the structure and morphology changes of graphene-supported $CoMn_2O_4$ bifunctional catalysts under practical rechargeable conditions. ACS Appl. Mater. Interfaces **6**, 16545–16555 (2014)
180. Lee, D.U., Park, M.G., Park, H.W., et al.: Highly active and durable nanocrystal-decorated bifunctional electrocatalyst for rechargeable zinc–air batteries. Chemsuschem **8**, 3129–3138 (2015)
181. Hu, Y., Han, X., Zhao, Q., et al.: Porous perovskite calcium–manganese oxide microspheres as an efficient catalyst for rechargeable sodium–oxygen batteries. J. Mater. Chem. A **3**, 3320–3324 (2015)
182. Yoon, K.R., Lee, G.Y., Jung, J.W., et al.: One-dimensional RuO_2/Mn_2O_3 hollow architectures as efficient bifunctional catalysts for lithium–oxygen batteries. Nano Lett. **16**, 2076–2083 (2016)
183. Jian, Z., Liu, P., Li, F., et al.: Core–shell-structured CNT@RuO_2 composite as a high-performance cathode catalyst for rechargeable Li–O_2 batteries. Angew. Chem. Int. Ed. **53**, 442–446 (2014)

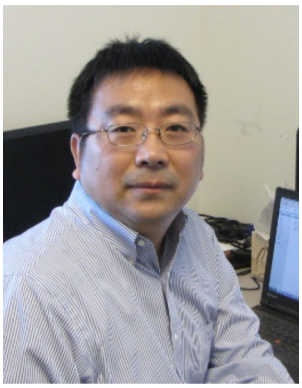

Dr. Yan-Jie Wang obtained his Ph.D. in Materials Science and Engineering from Zhejiang University, China, in 2005. Subsequently, he conducted two postdoctoral research positions at the Sungkyunkwan University, Korea, and at the Pennsylvania State University, USA, respectively. In 2009, he worked as a senior scientist at the University of British Columbia, Canada, in cooperation with the National Research Council of Canada and Vancouver International CleanTech Research Institute Inc., respectively. In 2017, he became a full-Professor at the Dongguan University of Technology, China. He is also an adjunct professor at the Fuzhou University. His interests include energy storage and conversion, polymer science, biomass, and medical areas.

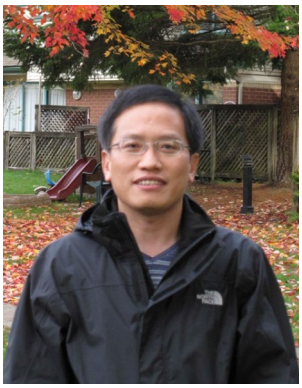

Dr. Baizeng Fang earned his Ph.D. in Materials Science from the University of Science and Technology, Beijing in 1997. He then worked as a postdoc in Holland, a JSPS fellow in Japan, a Lise Meitner scientist in Austria and a research professor at Korea University. He is a senior scientist at the University of British Columbia, Canada. He has published over 100 peer-reviewed papers in high-profile journals including the Journal of the American Chemical Society, Accounts of Chemical Research and Chemical Reviews. His research interests include nanostructured materials for electrochemical energy storage/conversion, and artificial photosynthesis. He also serves as an associate editor for RSC Advances.

Dr. Dan Zhang is a Lecturer at the Shanghai Institute of Mathematic and Mechanics at Shanghai University. Dr. Dan Zhang received her Ph.D. in Manufacturing Engineering of Aerospace Vehicle from the Northwestern Polytechnical University in 2006. Dr. Zhang's current research interests include the hydrodynamic of microfluidic devices and the reaction mechanism simulations of surface electrocatalysis in the field of fuel cells.

Dr. Aijun Li is currently a Professor at the School of Materials Science and Engineering at the Shanghai University (SHU). He received his Ph.D. in Materials Science from Northwestern Polytechnical University, Xi'an China in 2004. Dr. Li worked as a senior scientist and then a group leader for carbon materials at the Karlsruhe Institute of Technology (KIT), Germany from 2010 to 2015, being involved with the research, development and application of composites. Dr. Li's main research interests are in the complex interactions of multi-physical and chemical phenomena involved in chemically reacting flows; mainly focusing on modeling, simulation and synthesis of composites by chemical vapor infiltration/deposition processes.

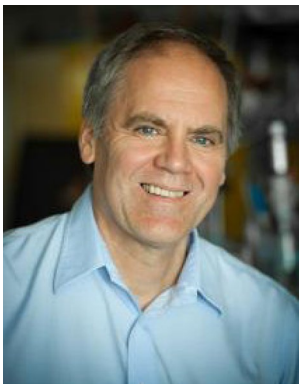

Dr. David P. Wilkinson is a professor and Canada Research Chair in the Department of Chemical and Biological Engineering at the University of British Columbia (UBC). He previously held the positions of Executive director of the UBC Clean Energy Research Center, Principal Research Officer and Senior Advisor with the National Research Council of Canada Institute for Fuel Cell Innovation, Director and Vice President of Research and development at Ballard Power Systems, and Group Leader at Moli Energy. His main research interests are in electrochemical and photochemical devices, energy conversion and storage materials, and processes to create clean and sustainable energy and water.

Dr. Anna Ignaszak is an Assistant Professor at the University of New Brunswick and an adjunct assistant professor at the Friedrich-Schiller University (Germany). She completed an appointment as a research associate at the Clean Energy Research Center, at the University of British Columbia (Canada), and as a research associate at the National Research Council of Canada. She has a diverse background in materials (carbons, composites, metal clusters) for electrochemical energy storage and conversion, electrochemical sensors, and heterogeneous catalysis. The research conducted in her laboratories in Canada and Germany aims to synthesize morphology-controlled catalysts, understanding the structure–reactivity interplay for optimum redox activity.

Lei Zhang is a Senior Research Officer at National Research Council Canada (NRC), a Fellow of the Royal Society of Chemistry (FRSC), an adjunct Professor of various Universities, and a vice president of International Academy of Electrochemical Energy Science (IAOEES). Lei's research interests include PEM Fuel Cell electrocatalysis, supercapacitors, metal-air batteries, batteries and hybrid batteries. She has co-authored more than 170 publications. She is the member of the NSERC Industrial R&D Fellowships College of Reviewers, the Editorial Board Member of Electrochemical Energy Reviews (EER) -Springer Nature. She is also an active member of the Royal Society of Chemistry (RSC), the Canadian Society for Chemistry (CSC), and the Canadian Society for Chemical Engineering (CSChE).

Dr. Jiujun Zhang is a Professor in College of Sciences, Institute for Sustainable Energy at Shanghai University. He was a Principal Research Officer at the National Research Council of Canada (NRC) from 2004 to 2016. Dr. Zhang received his B.S. and M.Sc. in electrochemistry from Peking University in 1982 and 1985, respectively, and his Ph.D. in electrochemistry from Wuhan University in 1988. He then carried out three terms of postdoctoral research at the California Institute of Technology, York University, and the University of British Columbia. Dr. Zhang has over 30 years of scientific research experience, particularly in the area of electrochemical energy storage and conversion. He is also the Adjunct Professor at the University of British Columbia and the University of Waterloo.